

Report

**R-23-16**

October 2024



# 3D geophysical and geological modelling for investigation of the Hudiksvall earthquake cluster

WP2 final report in the project "What is the cause of the Hudiksvall earthquake activity?"

**Stefan Luth**

**Peter Hedin**

**Stefan Bergman**

SVENSK KÄRNBRÄNSLEHANTERING AB

SWEDISH NUCLEAR FUEL  
AND WASTE MANAGEMENT CO

Box 3091, SE-169 03 Solna  
Phone +46 8 459 84 00  
skb.se

SVENSK KÄRNBRÄNSLEHANTERING



ISSN 1402-3091

**SKB R-23-16**

ID 2026322

October 2024

# **3D geophysical and geological modelling for investigation of the Hudiksvall earthquake cluster**

## **WP2 final report in the project “What is the cause of the Hudiksvall earthquake activity?”**

Stefan Luth, Peter Hedin, Stefan Bergman  
Sveriges geologiska undersökning

*Keywords:* Geophysical interpretation, Geophysical modelling, Structural geology, 3D modelling, Paleostress analysis, Bedrock map harmonization, Hudiksvall area.

This report concerns a study which was conducted for Svensk Kärnbränslehantering AB (SKB). The conclusions and viewpoints presented in the report are those of the authors. SKB may draw modified conclusions, based on additional literature sources and/or expert opinions.

This report is published on [www.skb.se](http://www.skb.se)

© 2024 Svensk Kärnbränslehantering AB



# Abstract

In this report we describe the activities and results within work package 2 of the SKB-project “What is the cause of the Hudiksvall earthquake activity?”

The method of harmonization of bedrock map data at SGU is described and the results from harmonization of bedrock polygons and deformation zone lines are presented. A large number of geological structures (ductile, brittle-ductile and brittle) were observed and measured in the field. The collected kinematic data from faults was then used for paleostress analysis using existing methods. The results are in line with previous studies in central Sweden, with the interpretation that faults were active during north to northeast compression at 1.7–1.6 Ga and northwest to west–northwest compression at 1.1–0.9 Ga.

Geophysical maps have been prepared from airborne magnetic and electromagnetic data as well gravity data. New interpretations of magnetic lineaments and connections that are presented here are used to outline an anomalous, elongate, diffuse zone, oriented NNE–SSW, that coincides with the earthquake cluster around Hudiksvall.

Three-dimensional models based on magnetic and gravity data were inverted independently and constrained by petrophysical results. The presented 3D geological models are largely based on the bedrock map of Sweden at 1:1 million, but also utilize the geophysical modelling results, structural field data, and interpretations derived from pre-existing, but recently reprocessed seismic lines (BABEL and UPPLAND). The combined models reveal a north–east striking and north–west dipping fault system, here introduced as the Hudiksvall fault. We propose that the fault itself, as well as its intersection with the Hassela shear zone, may play a significant role in producing and localizing the earthquakes in this region.

# Sammanfattning

I denna rapport beskriver vi aktiviteter och resultat från arbetspaket 2 i projektet ”Vad är orsaken till jordbävningsaktiviteten i Hudiksvallsområdet?”.

Metoden för harmonisering av berggrundskartdata vid SGU beskrivs och resultat från harmonisering av berggrundsytor och deformationszonslinjer presenteras. Under strukturgeologiskt fältarbete observerades, beskrevs och mättes såväl plastiska och spröd-plastiska som spröda strukturer, och kinematiska data samlades in. Informationen från förkastningar användes för att göra paleospänningsanalys med befintliga metoder. Resultaten överensstämmer med tidigare studier i centrala Sverige, och tolkningen är att förkastningar var aktiva under nordlig till nordostlig kompression för 1,7–1,6 miljarder år sedan, och under nordvästlig till väst–nordvästlig kompression för 1,1–0,9 miljarder år sedan.

Kartor har tagits fram från data från flygburna magnetiska och elektromagnetiska mätningar och från tyngdkraftsmätningar. Nya tolkningar av magnetiska lineament och konnektioner presenteras här, och används för att påvisa ett diffust, avlångt område, i riktning NNO–SSV, som verkar sammanfalla med jordbävningsklustret.

Tredimensionella modeller baserade på mätresultat av det magnetiska fältet och tyngdkraftsfältet har tagits fram. Petrofysiska data har använts som stöd. För 3D-modellering av berggrundsenheter och strukturer som veck och större deformationszoner har även fältmätta strukturer och seismiska modeller använts. Vid tolkningen framkom en nordostligt strykande och nordvästligt stupande zon med förkastningar, här benämnd Hudiksvallsförkastningen. Vi föreslår att denna förkastning och dess skärning med Hasselaskjuvzonen kan vara betydelsefulla för uppkomsten och lokaliseringen av jordbävningarna i området.

# Contents

<b>1</b>	<b>Introduction</b>	7
<b>2</b>	<b>Geological setting</b>	9
<b>3</b>	<b>Harmonization of map data</b>	13
<b>4</b>	<b>Geological structures in outcrop</b>	17
4.1	Ductile deformation	18
4.2	Brittle-ductile deformation	19
4.3	Brittle deformation	19
<b>5</b>	<b>Paleostress analysis from fault-slip data</b>	25
5.1	Methodology for paleostress analysis	25
5.2	Results of the paleostress analysis	25
5.3	Conclusions from the paleostress analysis	28
<b>6</b>	<b>Geophysical modelling</b>	29
6.1	Input data	29
6.1.1	Airborne geophysics	29
6.1.2	Gravity	32
6.1.3	Petrophysics	32
6.2	Results	34
6.2.1	Interpretation of aeromagnetic data	34
6.2.2	Interpretation of gravity data	37
6.2.3	3D geophysical modelling	37
<b>7</b>	<b>3D geological modelling</b>	45
7.1	Crustal model of the Ljusdal lithotectonic unit	45
7.1.1	Input data, methods used and resulting crustal model	45
7.2	Lithology model of the Hudiksvall area	48
7.2.1	Input data, methods used and resulting lithology model	48
<b>8</b>	<b>Discussion and Conclusion</b>	53
8.1	The “Hudiksvall fault”	54
8.2	Recommendations for future work	56
	<b>References</b>	57
	<b>Appendix</b>	59



# 1 Introduction

The earthquake cluster in the Hudiksvall area has not yet been correlated with any distinct geological feature, such as an old deformation zone or younger postglacial fault. This report describes the work done by SGU in the years 2021–2023 within the project “What is the cause of the earthquake activity in the Hudiksvall area? The project also includes establishment of a dense temporary seismic network (Uppsala University) and Quaternary geological investigations (SGU).

The report starts with an introduction to the bedrock geology of the study area around Hudiksvall (Figure 2-1), the extent of which was chosen to include the vast majority of earthquakes recorded between 2000 and 2018. Then follows an account on the harmonization of the bedrock map that has been made. Chapters 4 and 5 show the results of structural geological field work and the processing and interpretation of fault slip data in terms of a paleostress analysis. Modelling is the theme of the Chapters 6 and 7, where geophysical and geological input data, the modelling methods and the results are described. In the closing Chapter 8, combined geophysical and geological interpretations are presented and discussed followed by recommendations for future work which are reported separately.



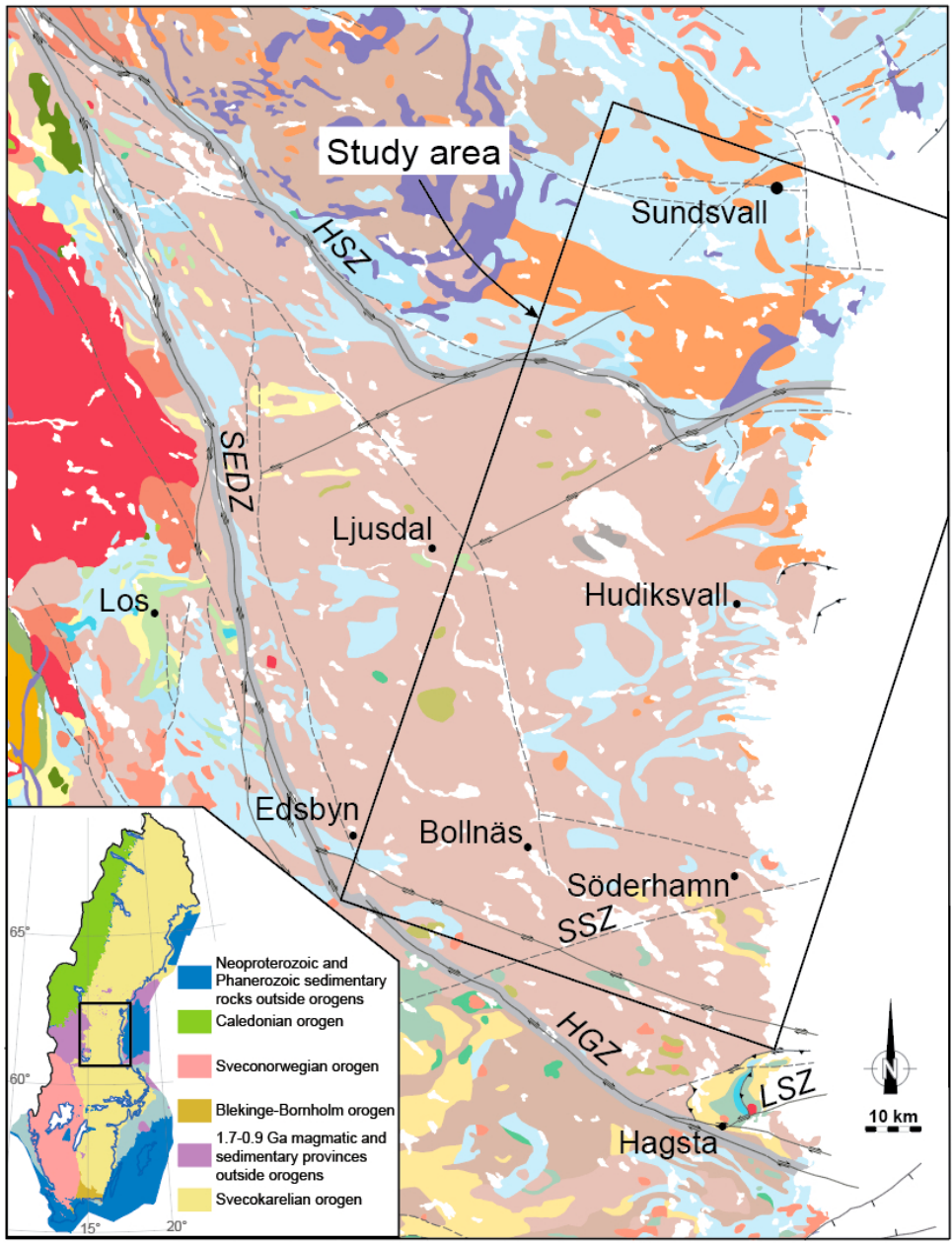
## 2 Geological setting

The main part of the bedrock in the study area belongs to the Ljusdal lithotectonic unit (LTU; Högdahl & Bergman 2020) and the Bothnia-Skellefteå lithotectonic unit, both in the 2.0–1.8 Ga Svecokarelian orogen, see Figure 2-1. Younger events have to a variable degree affected rocks belonging to the Svecokarelian orogen by intrusive activity, fracturing, hydrothermal alteration etc. The most important events in surrounding areas include the 1.7–1.5 Ga Gothian orogeny, the 1.5–1.4 Ga Hallandian orogeny, the 1.1–0.9 Ga Sveconorwegian orogeny and the 0.5–0.4 Ga Caledonian orogeny (Stephens 2020). A summary of the stress field evolution was presented by Viola et al. (2009) and is summarized here. During the late stages of the Svecokarelian orogeny, and possibly also the Gothian orogeny, fractures record two compressional shortening events, oriented approximately NW–SE to NNW–SSE and NNE–SSW. Compression in an approximately E–W direction occurred during the Sveconorwegian orogeny, while Caledonian shortening was oriented approximately NW–SE to E–W. Permian trans-tension was oriented NE–SW, while shortening events possibly related to the Laramide and Alpine orogenies were oriented approximately NE–SW and NW–SE.

The LTU is bound to the north by the Hassela shear zone (HSZ, Sjöström et al. 2000) from the Bothnia-Skellefteå lithotectonic unit and by the Storsjön-Edsbyn deformation zone (SEDZ, Bergman et al. 2006) and Hagsta gneiss zone (HGZ, Högdahl et al. 2009) from the Bergslagen lithotectonic unit in the west and south. To the east, under the Bothnian Sea, the LTU is overlain by Mesoproterozoic to Ordovician sedimentary rocks. Dextral movement was dominant in the deformation zones, but dip-slip movement was also important, especially in the Storsjön-Edsbyn deformation zone. Deformation zones also occur within the LTU, e.g. the Lindön shear zone (LSZ) (Figure 1-1, Bergman & Sjöström 1994).

The LTU is composed of deformed and variably metamorphosed intrusive rocks, with an age of 1.87–1.84 Ga, belonging to the Ljusdal batholith. Within the batholith there are supracrustal belts or inliers made up of mainly migmatitic metasedimentary and metavolcanic rocks. Amphibolite is a subordinate component in the supracrustal sequences. In the Hamrånge area at Hagsta (Figure 2-1), the rocks are better preserved, and primary structures are common. Granite and pegmatite occur as dikes and small massifs throughout the area.

The northern part of the study area belongs to the Bothnia-Skellefteå lithotectonic unit (Skyttä et al. 2020). It is dominated by migmatitic metasedimentary rocks and variably metamorphosed granitoids. North of the Hassela shear zone there are large areas with dolerite, both as steep dikes and as gently dipping sheets in the older bedrock. Glassy rocks of mainly rhyolitic composition are found WNW of Hudiksvall. They were probably formed by melting of the older bedrock caused by a meteorite impact (Svensson 1968).



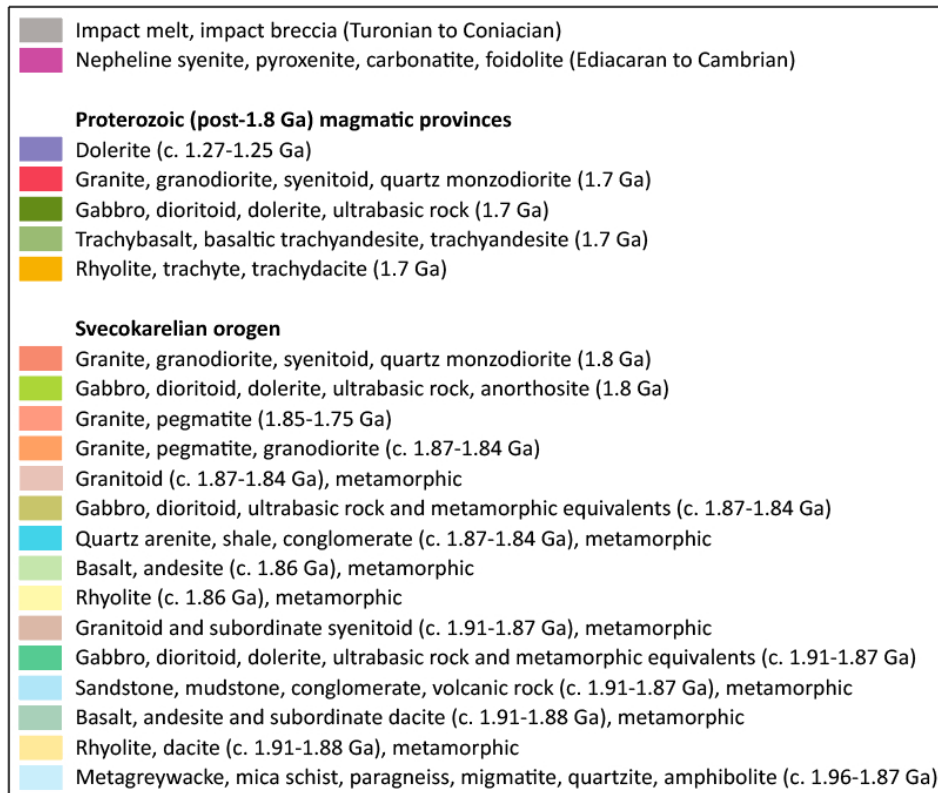


**Figure 2-1.** The bedrock in and around the Ljusdal lithotectonic unit. The thick gray line follows the deformation zones that envelop the unit: HSZ = Hassela shear zone, SEDZ = Storsjön-Edsbyn deformation zone, HGZ = Hagsta gneiss zone. Other abbreviations: SSZ = Söderhamn shear zone, LSZ = Lindön shear zone. The unit north of HSZ is the Bothnia-Skellefteå lithotectonic unit. The black rectangle shows the location of the study area. The inset map shows the major lithotectonic units in Sweden and the location of the main map. The maps are modified from *Bedrock 1:1 million* (SGU 2021a).



### 3 Harmonization of map data

The map database “Bedrock 1:50 000–1:250 000” at SGU contains the results of bedrock mapping and interpretation of analytical results and geophysical data that started in the 1960’s and which is still ongoing. During these more than 60 years the mapping methods have changed. The intended presentation scales and observation point densities have also been different in different areas. Considering these factors together it is natural that there is a large variation in quality within the database. This can to some degree be overcome by geometric and semantic harmonization, supported by field check.

The maps covering the Hudiksvall area were published from 1987 to 2008, see Figure 3-1, and the bedrock map before and after harmonization is shown in Figure 3-2A–D. When the original maps placed side by side major changes in color appear at map boundaries (Figure 3-2A). There are two main reasons for this. The first reason is that the accumulation of radiometric age determinations from the 1990’s and onwards made it clear that the oldest group (c. 1.9 Ga) of mainly granitoid intrusions in central Sweden (named e.g. Urgranit series, primorogenic intrusions) had a large age span and needed to be subdivided into two separate age groups, 1.92–1.87 Ga and 1.87–1.84 Ga, respectively. The age groups were assigned different map portrayal colors and the subdivision was applied in the present area after year 2005. The second reason is a change by SGU of how metamorphic rocks, especially migmatites, are described and portrayed on maps. Previously emphasis was put on the original character of the rock, and thus terms and map colors were chosen to reflect the protolith. The drawback of this was that lithologies that are very different in appearance, e.g. migmatitic paragneiss and cross-bedded sandstone, had the same map color. From about year 2005 diatexitic migmatite was portrayed in a certain way, irrespective of protolith. This is the main reason for map boundary problems in the Sundsvall area.

The location and properties of deformation zones (ductile and brittle-ductile shear zones, brittle faults and fracture zones) on maps are mainly the results of interpretations of geophysical and elevation data and to a very small extent by field observation. The inherent subjective component in interpretation inevitably leads to mismatch along map boundaries. Other contributing factors include variable contrasts in elevation and geophysical properties and changes of methodology and coverage of the completed investigations. SGU distinguishes lineaments (linear features without genetic connotations) from deformation zones (linear features interpreted as geological structures) and they belong to different classes in the present data model. This distinction was not clear in previous models which led to misclassification during transformation into the present model. In most areas without lines in Figure 3-2C, reclassification of lineaments to deformation zones could be done. SGU now has a rule that deformation zones shorter than 5 km should generally not be shown on standard 1:50 000 scale maps, unless they are important in controlling lithological boundaries. Some lines less than 5 km in length have therefore been removed. Misfits along map boundaries have been corrected by minor geometrical modification such as moving parts of lines and adding or deleting short segments. In the entire study area, superfluous lines were removed, and gaps and overshoots were corrected.

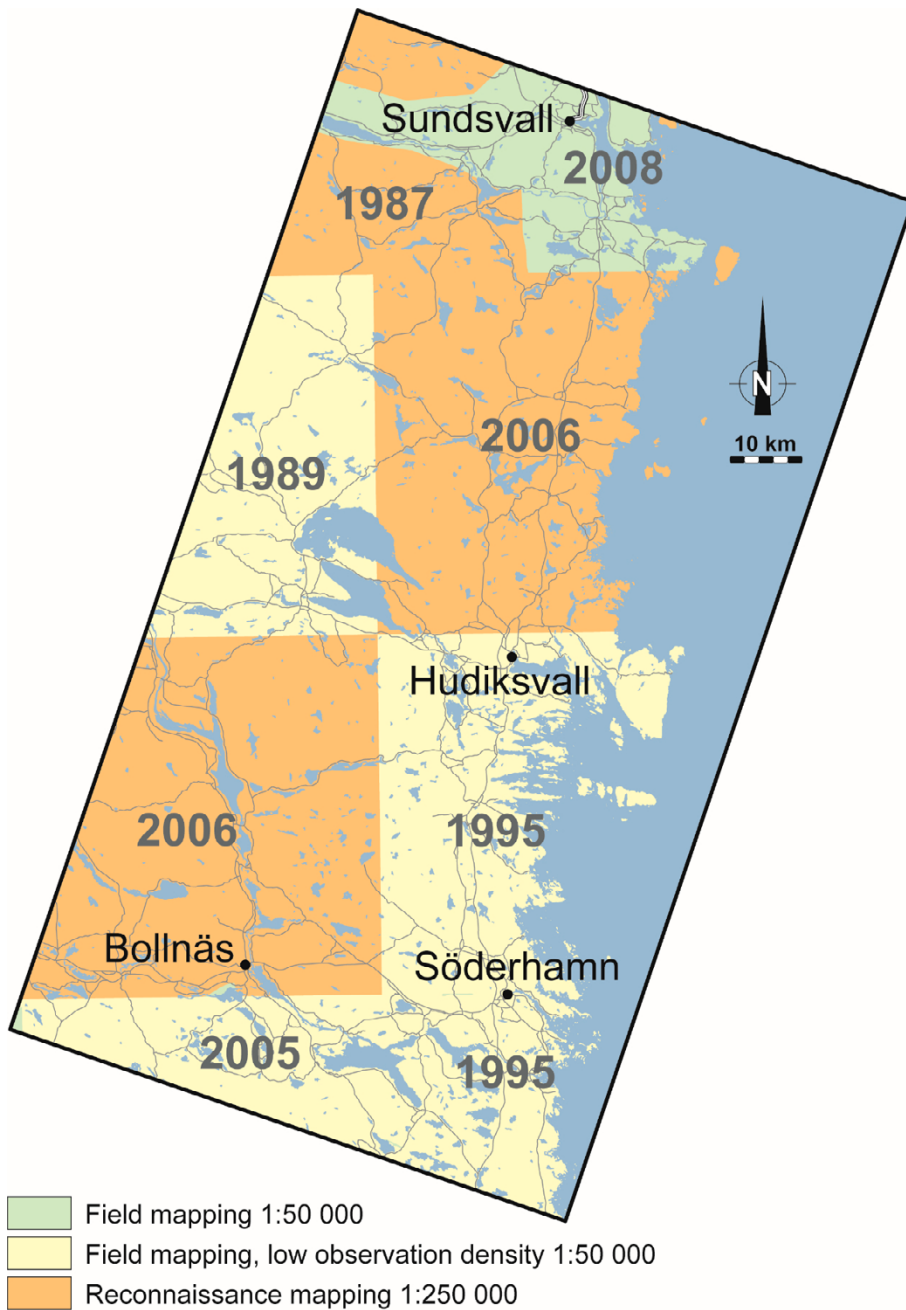


**Figure 3-1.** Geological map sheets and their year of publication within the study area. The different colors represent the mapping methods that were used in the respective areas. Gray numbers show the years of map publication. The map is modified from SGU (2021b).

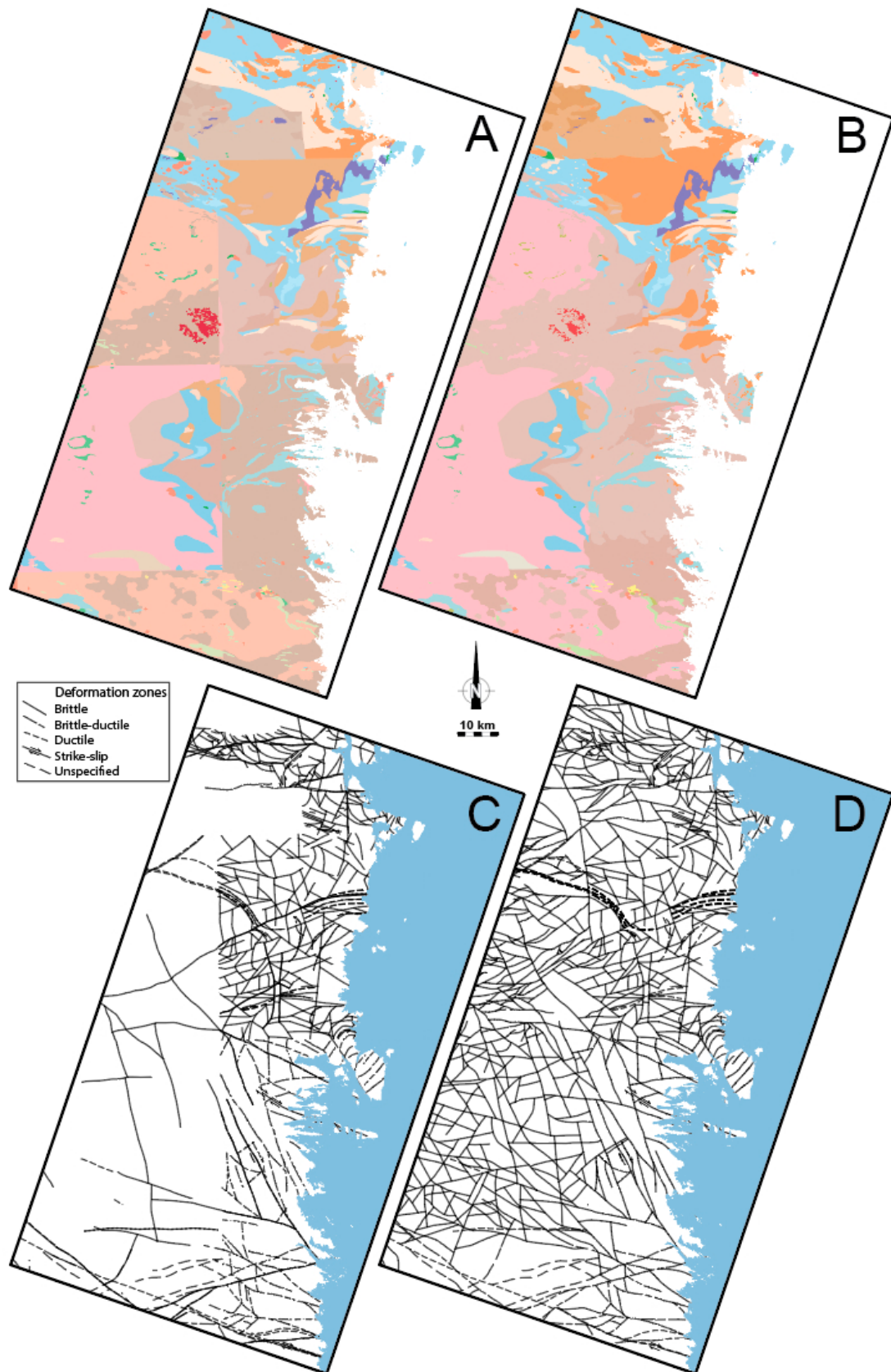


**Figure 3-2.** Bedrock polygons in the SGU map database “Bedrock 1:50 000–1:250 000” (SGU 2021b). (A) before and (B) after harmonization. Likewise, the maps C and D show deformation zones in the same database before and after reclassification and harmonization.



## 4 Geological structures in outcrop

Geological observations were made on 48 outcrops including 4 quarries (Figure 4-1). Most visited outcrops are located within the Hudiksvall earthquake cluster whereas a smaller number is located along its periphery. The bulk of the studied outcrops were roadcuts measuring several tens of meters in length and including good exposures that were used to measure the orientation of a large number of ductile, but primarily brittle structures, such as faults, fractures, and slip lines (slickenlines). The obtained structural datasets were then used to unravel consistent local and regional deformation patterns, and to reconstruct fault kinematics and paleostress fields within the Hudiksvall earthquake cluster.

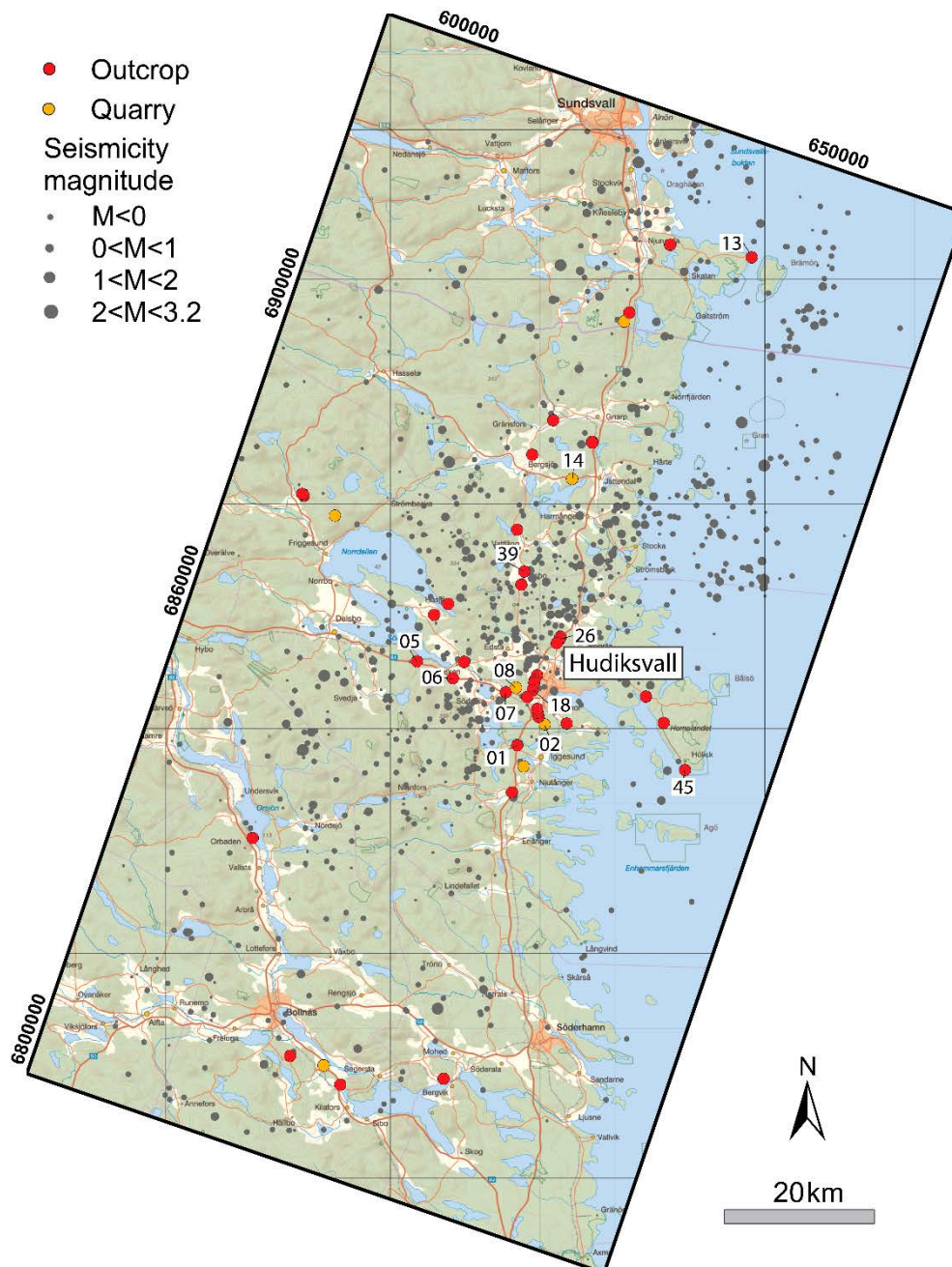


**Figure 4-1.** Distribution of studied outcrops and quarries plotted together with the epicentre of earthquakes recorded between 2000 and 2018 recorded by SNSN. Labels indicate outcrop ID without the prefix “SLH2100”. Only the labels of localities which are referred to in the text or displayed photos are included. See Table A-1 for associated coordinates.

## 4.1 Ductile deformation

Ductile deformation within the Ljusdal lithotectonic unit is in general polyphase and comprises three separate folding phases (e.g., Ogenhall & Sjöström 2010, Högdahl & Bergman 2020). The associated structures vary in style and orientation within the unit from east to west, which is also evident from the magnetic anomaly patterns (Figure 6-1). In general, the boundary zones of the LTU in south, west and north are marked by strong shearing and faulting, whereas large-scale folding is more evident in the east. Around the city of Hudiksvall, the high-grade metamorphism caused migmatitization of both magmatic and sedimentary rocks, which makes the identification of separate folding phases difficult. On the outcrop scale, however, ductile deformation within the metatexites is expressed by a penetrative foliation or gneissic banding ( $S_1$ ), which is locally folded, boudinaged, and disrupted into schollen bounded by large volumes of leucosome (Figure 4-2). The orientation of the foliation varies locally and has not been measured systematically in this study. Nevertheless, the stereographic projection of the poles from the in total 18 measured foliations appear to plot on a great circle that is consistent with the regional  $F_3$  folding trend along steep, east–west axial surfaces (see also Figure 4-7, and Högdahl & Sjöström 2001).

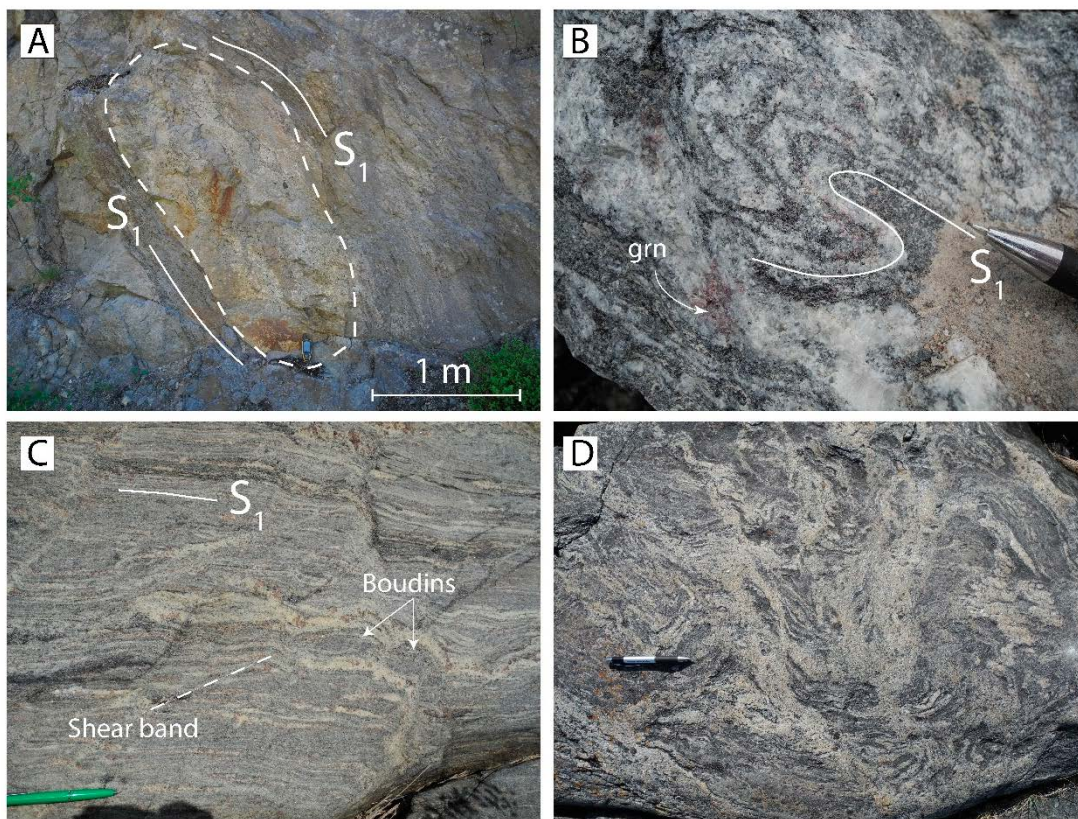


**Figure 4-2.** Character of ductile structures in migmatites around Hudiksvall. A) Main foliation ( $S_1$ ) folding around a competent gneissic lens/boudin. Outcrop SLH210039. B) Asymmetric folding of metatexite with garnet (grn) in the melt rich parts. Outcrop SLH210008. C) Banded metatexite with additional leucosome along shear bands and boudin necks. Outcrop SLH210045. D) Folded schollen of metatexite bounded by younger leucosome. Outcrop SLH210013. Photographs: S. Luth.

## 4.2 Brittle-ductile deformation

The few brittle-ductile deformation zones observed in this study are characterized by a 10 to 50 cm thick core which exhibits clear signs of ductile deformation and mylonitization, with deformation becoming more brittle towards the edges (Figure 4-3). Kinematic indicators, including sigma clasts, shear bands and S-C fabrics are developed only locally in the core zone, whereas feldspar is typically deformed in a brittle manner, indicating temperatures during deformation reaching below 350 °C. The orientation of brittle-ductile deformation zones varies from sub-horizontal (Figure 4-3A) towards steeply dipping. However, the observed zones were too few to reveal a regional trend.

## 4.3 Brittle deformation

Brittle deformation throughout the area is expressed by the local development of brittle deformation zones, faults, fracture zones and fracture sets (Figures 4-4 to 4-6). Fractures are distinguished from faults in a way that the former reveal no evidence for movements along the plane. The brittle deformation zones are up to 5 m thick and are filled with highly fractured rock, broken clasts and fault gouge (Figure 4-4C–D). The brittle deformation zones often contain multiple fault planes. Minor faults and fractures are typically up to 5 cm thick and either filled with quartz, calcite, laumontite, prehnite, chlorite or lack fracture filling (Figure 4-5A–C). In a single observation, located along the E4 motorway at Hudiksvall, the fault plane is associated with pseudotachylyte (Figure 4-5D). A large number of fault surfaces contain slickensides (Figure 4-5E–F). The bulk of the observed fractures can be subdivided into single fractures or fractures that are part of a fracture set or more locally, fracture zones (Figure 4-6A–F).

The structural measurements are plotted in stereonet (Stereonet 11, Allmendinger et al. 2012, Cardozo & Allmendinger 2013) for each structure type to determine local and regional structural trends (Figure 4-7). The poles of the main foliation plot along a great circle, despite a relative low number of measurements. The brittle deformation zones, again few in amount, plot with an average orientation of steeply dipping and NE-striking. A similar averaged orientation is derived from fault planes, albeit based on a large number of measurements that hardly reveal any clustering. In contrast, the bulk orientation for the disperse pattern of fractures is steeply dipping but striking almost north–south. An almost likewise spread in trend and plunge is apparent from the plotted fault slip lines (slickensides).

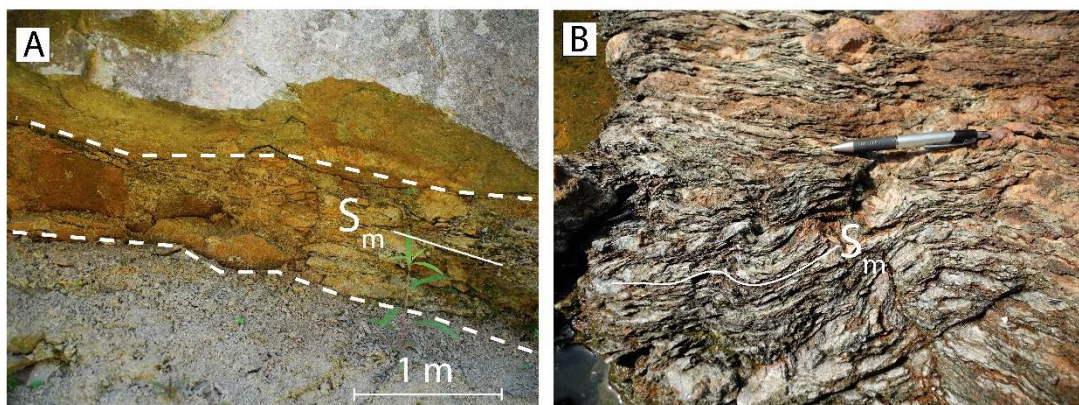


**Figure 4-3.** Brittle-ductile deformation zone in outcrop. A) A c. 50 cm thick core zone contains a mylonitic foliation ( $S_m$ ) and is bounded by brittle fault planes (dashed lines). Outcrop SLH210026. B) Folding of mylonitic foliation ( $S_m$ ) within a 1-meter-thick brittle-ductile deformation zone. Outcrop SLH210013. Photographs: S. Luth.

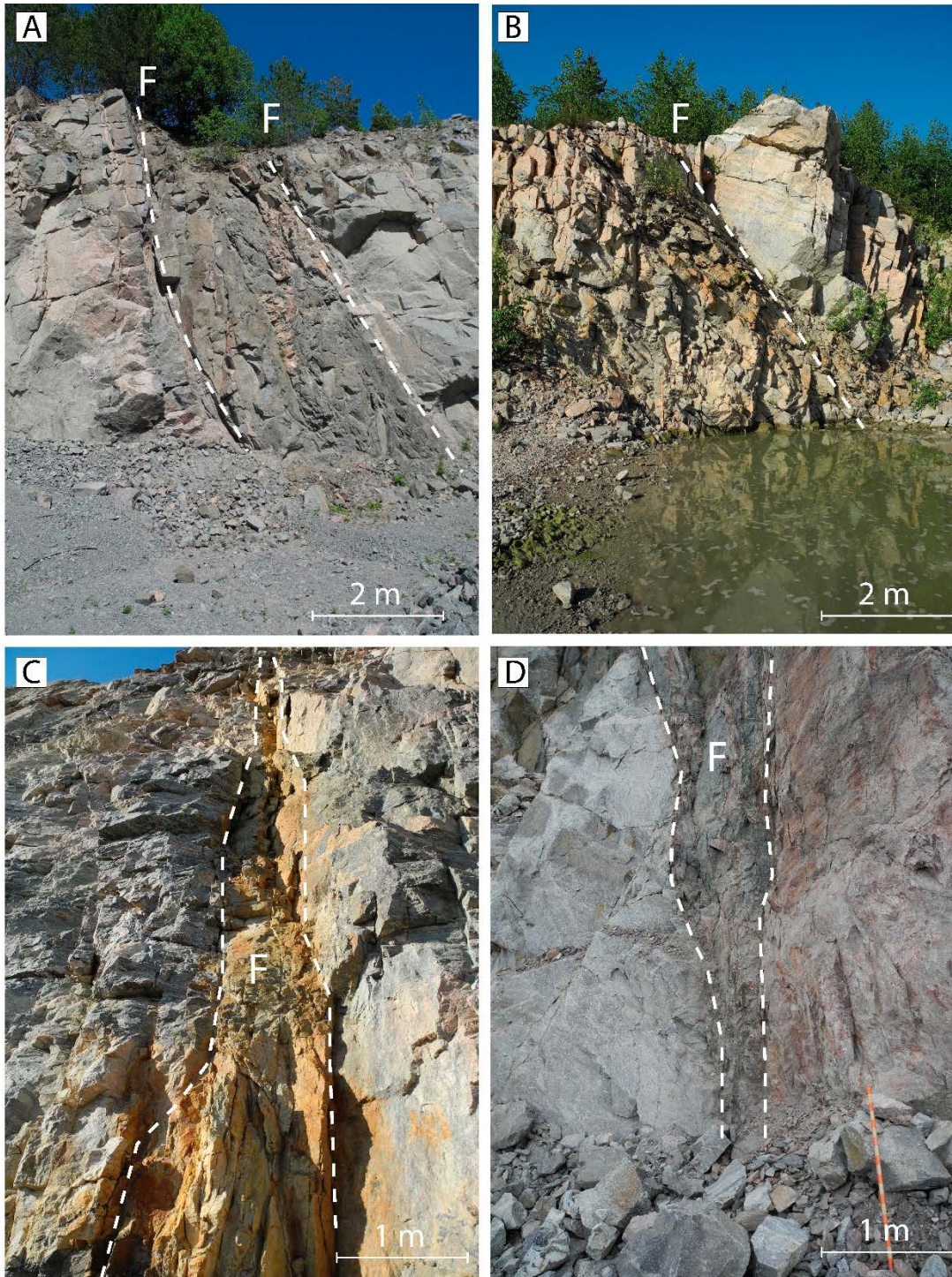


**Figure 4-4.** Character of brittle deformation in quarries around Hudiksvall. A) Brittle deformation zone bounded by two faults dipping steeply to moderately towards the SE (dashed lines). Outcrop SLH210002. B) Strongly fractured brittle deformation zone bounded by a single fault dipping  $60^\circ$  towards the SE (dashed line). Outcrop SLH210014. C) Steeply dipping fault (dashed line) comprising highly fractured rock and fault gouge. Rusty color is caused by oxidation of iron. Outcrop SLH210014. D) Steeply dipping fault (dashed line) comprising highly fractured rock and fault gouge. Notice the variable thickness of the fault (between dashed lines) in both C and D. Outcrop SLH210008. Photographs: S. Luth.

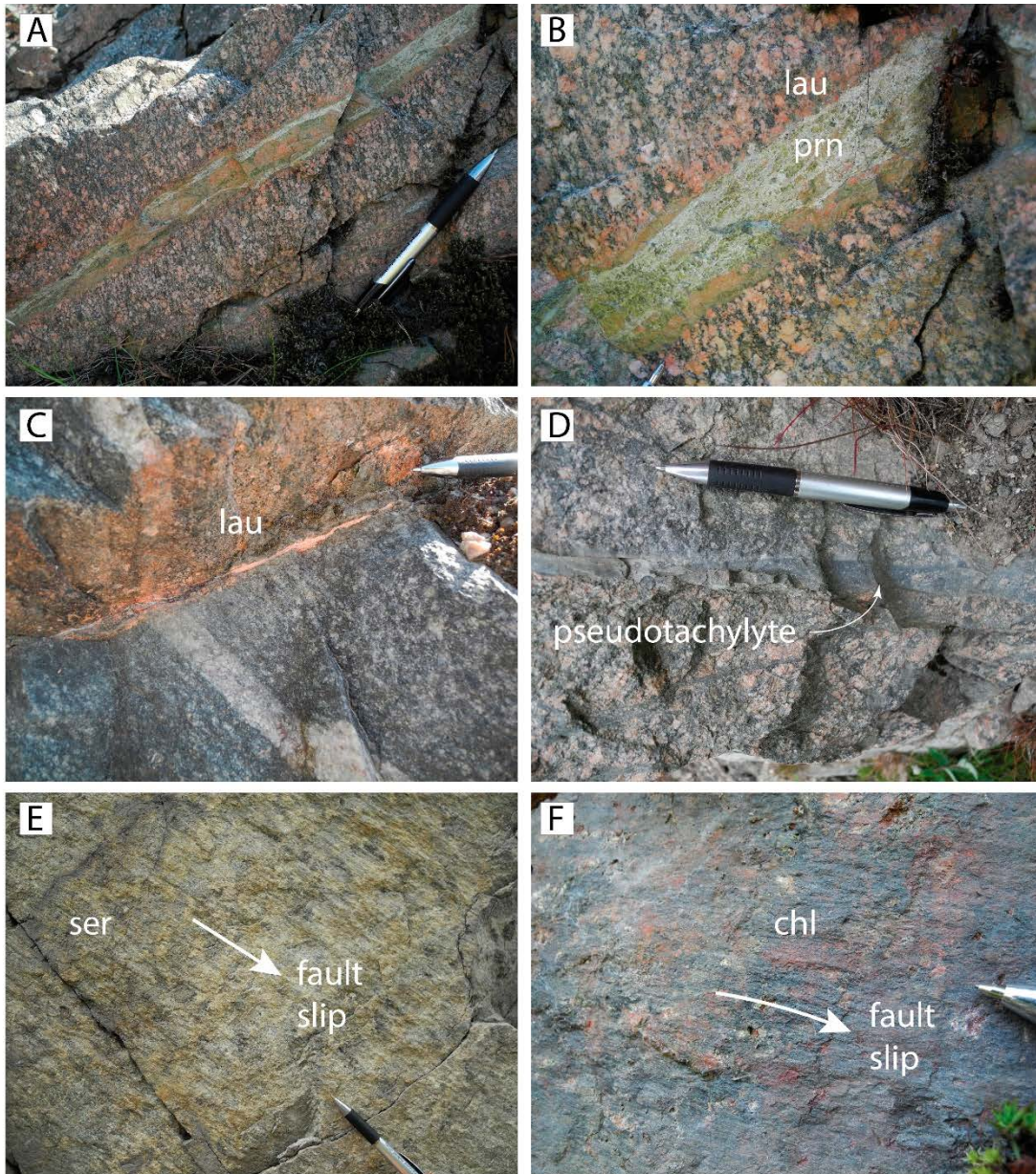


**Figure 4-5.** Character of brittle deformation in outcrops in the Hudiksvall study area. A) Fault filled with prehnite (prn, pale greenish) with a laumontite halo within a feldspar-phyric metagranitoid. Outcrop SLH210001. B) Close-up of (A). C) Narrow fracture filled with primarily laumontite (lau, pinkish). Outcrop SLH210001. D) NE-striking and steeply dipping pseudotachylyte within mylonitized and brecciated migmatite. Outcrop SLH210018. E) Slickensides on fault plane comprised probably of sericite (pale green). Downwards stepping indicates hanging wall down movements. Outcrop SLH210007. F) Slickensides on fault plane comprised of chlorite (blackish). Downwards stepping indicates hanging wall to the right movements. Outcrop SLH210006. Photographs: S. Luth.



**Figure 4-6.** Character of fractures in outcrops in the Hudiksvall study area. A) Gently dipping fractures intersected by a set of vertical fractures. Outcrop SLH210005. B) Steeply dipping, NE-striking fractures at a high angle to the gently dipping metamorphic banding (S1). Outcrop SLH210045. C) Fracture zone comprising multiple anastomosing and branching fractures. Outcrop SLH210045. D) N-S striking fracture filled by pegmatite. Outcrop SLH210045. E) Steeply dipping, NE-striking fracture zone. Outcrop SLH210045. F) Vertically dipping, N-S striking fracture zone outlining a graben morphology. Outcrop SLH210013. Photographs: S. Luth.

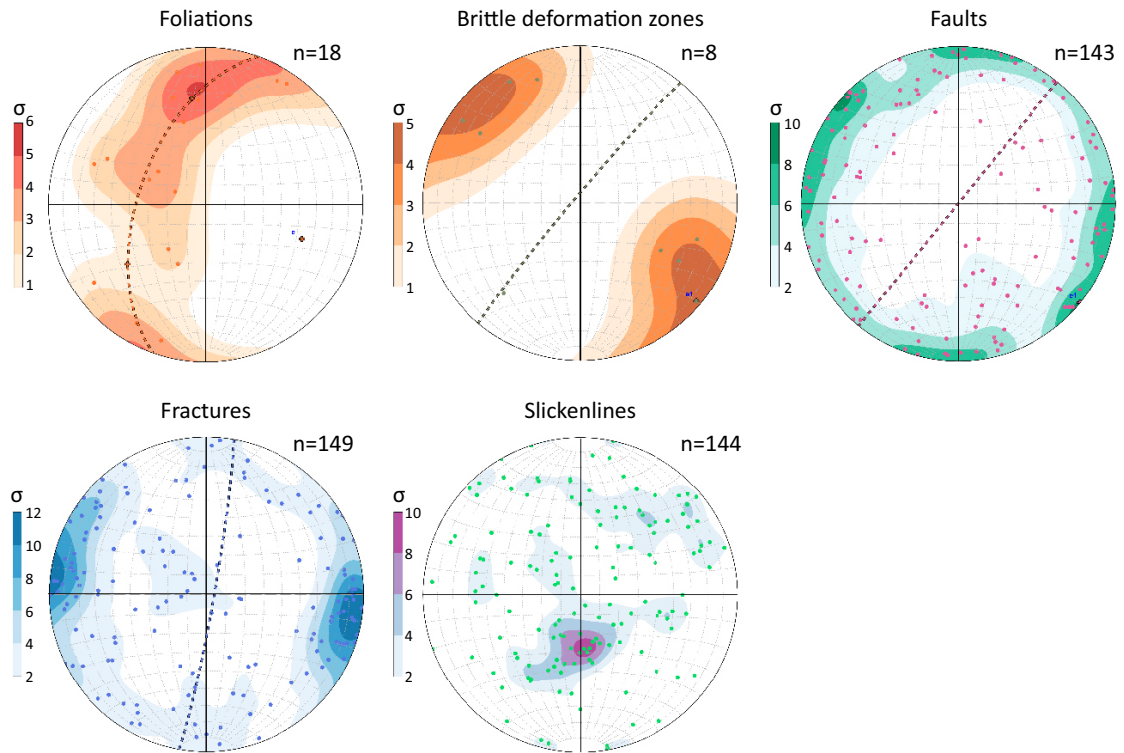


**Figure 4-7.** Lower-hemisphere, equal area stereonet projections of geological structures measured for this study in outcrops around Hudiksvall (see Figure 4-1). Planes are plotted as poles (colored dots). Dashed line indicates calculated average plane for the brittle deformation zones, faults and fractures. The dashed line in the foliation stereonet represents the axial surface, the pole (cross) of which indicates the fold axis. Contouring of data is at a  $2\sigma$  significance level using exponential Kamb. Notice the large scattering in the orientation of faults, fractures and slickenlines, which is somehow required in obtaining a stable paleostress tensor (see next section).



## 5 Paleostress analysis from fault-slip data

Brittle deformation throughout the study area has been recorded by the large number of brittle faults and fractures. The direction of slip along the frictional planes is in many cases preserved by slicken-sides consisting of quartz, laumontite or chlorite, which allow for the determination of the orientation of the principal stresses.

### 5.1 Methodology for paleostress analysis

We performed a paleostress analysis by using the free software WinTensor version 5.8.5 (see also Delvaux & Sperner 2003), which includes the right dihedron method (Angelier & Mechler 1977) and rotational optimization to refine the calculated tensor. The tensor quality, ranging from A (very good) to E (very poor) depends on the number of measurements, the average slip deviation angle, the confidence level of the field measurement and the variety of measured orientations (Delvaux & Sperner 2003). The size of bedrock exposure as well as the amount of collected structural data varies heavily throughout the study area. Therefore, fault data from neighbouring observations were sometimes combined into a single outcrop cluster. The variety of plane and slip orientations was often high, which is beneficial in order to calculate a stable, high-quality tensor. Overprinting relations between the faults have not been recognized in the field. A subdivision in different sets, relating to separate deformation phases, is therefore solely based on the paleostress analysis.

### 5.2 Results of the paleostress analysis

The outcome of the paleostress analysis is shown in Figures 5-1 and 5-2, which includes the final stereonet per outcrop cluster after rotation optimization, the principal stress axes, mean maximum horizontal compression direction ( $Sh_{max}$ ) and the mean minimum compression direction ( $Sh_{min}$ ), and the quality rank. Each plot also includes a graph of the optimization function F5, which consists of two terms. The first term exploits the directional part of the resolved shear stress (orientation and sense) for minimizing a misfit angle and the second term exploits the resolved magnitudes for optimizing the resolved normal and shear stresses magnitudes to favor slip on the plane (see for more details: WinTensor 2023).

The result can be categorized into two groups: 1) N to NE directed tension and 2) N to NE compression. Group 1 can be subdivided into clusters revealing radial extension (clusters 3 and 6), pure extension (2), and transtensional with WNW to NW compression (1,7,4). Likewise, group 2 can be subdivided into radial compression (5), transpressional with WNW tension (6 set 2) and pure compressional (5 set 2, 8). We attribute the slight variation among tensors in a single group to local disturbances in the stress field as well as to rotation during deformation within a single tectonic stage.

The resulting quality rank is relatively poor, in particular, the E quality of cluster 7, which means that the result is not reliable. It does not mean that the data are not reliable, but that the data set does not meet the requirement expressed by these parameters. It can be that the number of data used is too small, that they have a poor spatial dispersion or that the sense of movement is not well defined.

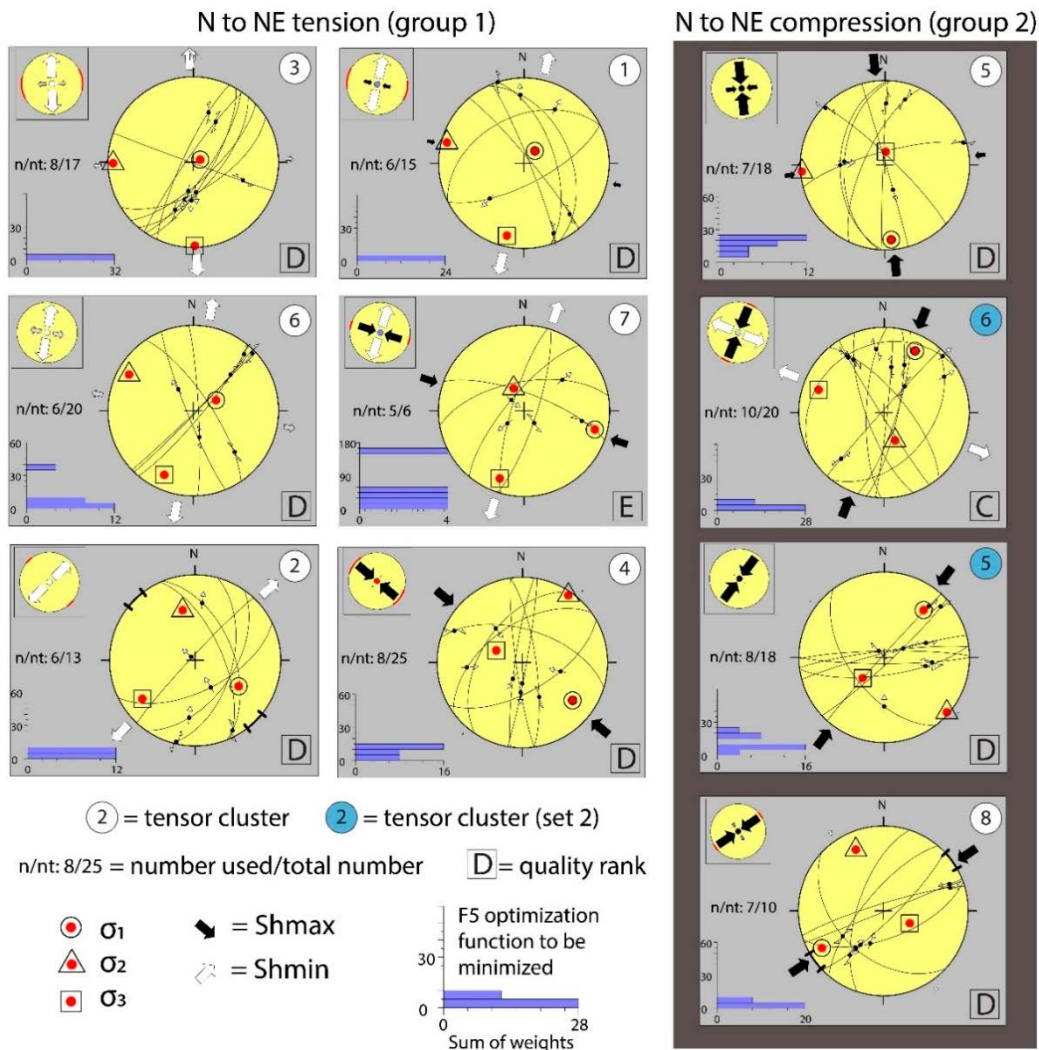


**Figure 5-1.** Results of the paleostress analysis per cluster after rotation optimization. See text for more details. Information on the location of each cluster and used data is included in Figure 5-2 and Table A-2.

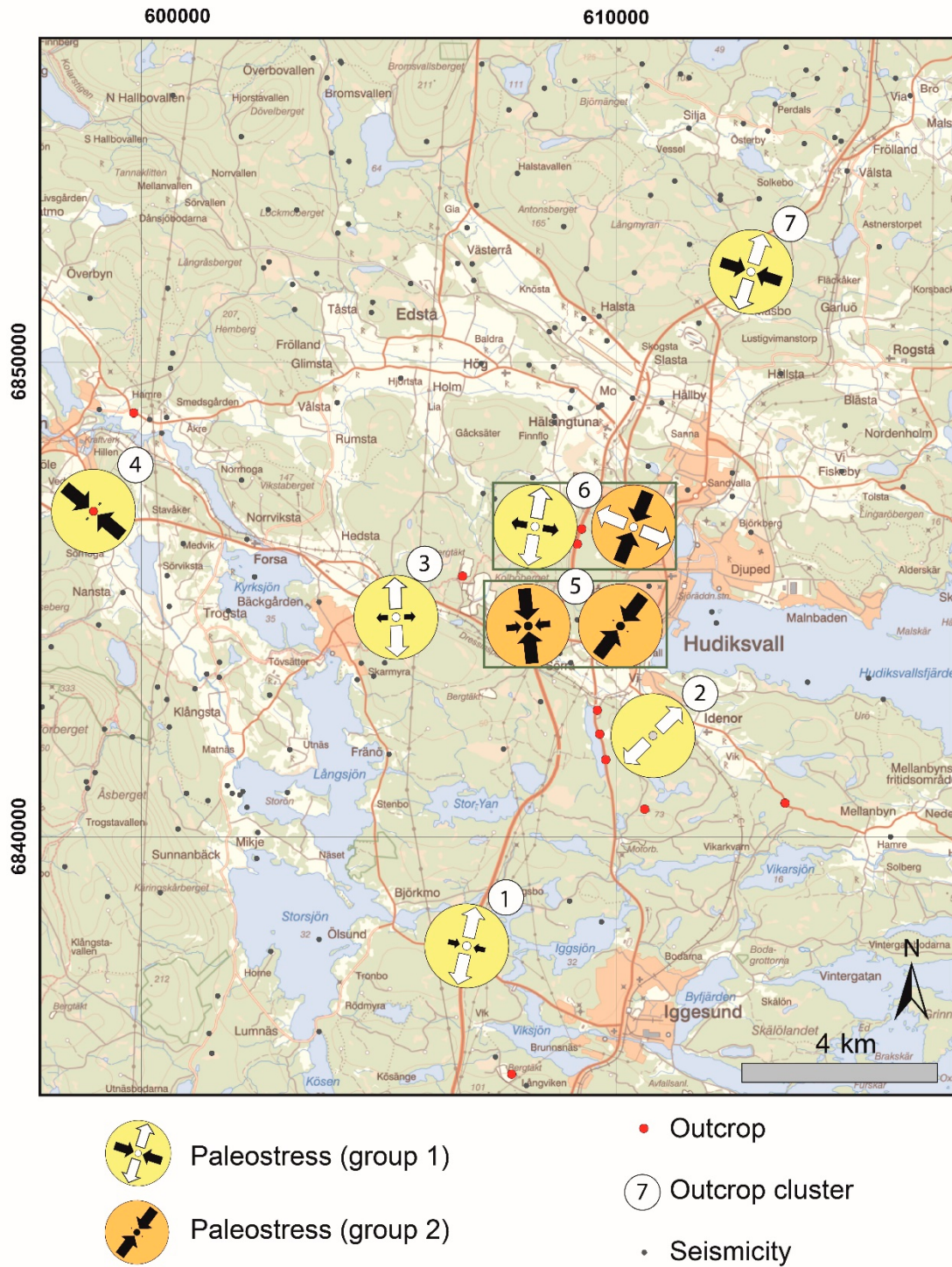


**Figure 5-2.** Location of fault-slip data clusters used for paleostress analysis. Arrows refer to the resulting mean maximum horizontal compression direction ( $Sh_{max}$ ) and the mean minimum compression direction ( $Sh_{min}$ ). Different coloring of stereonet refers to the two resulting groups (see also Figure 5-1). Notice that clusters 5 and 6 produced two subsets with significant (6) or slight (5) differences in horizontal stress directions. Information on the location of each cluster and included measurements are listed in Tables A-1 and A-2, respectively.

### 5.3 Conclusions from the paleostress analysis

Despite the low-quality ranking of the derived paleostress tensors (very poor to acceptable), we do observe a rather consistent regional paleostress pattern, which is compatible with the results from regional investigations on brittle deformation throughout the Nordic countries (e.g Stephens et al. 2007, Söderbäck 2008, Viola et al. 2009, Saintot et al. 2011).

In this perspective, we interpret the paleostress field represented by N to NE compression (group 2) to be mechanically compatible with NE bulk crustal shortening between 1.7 and 1.6 Ga (Gothian). A regional paleostress field with N to NE tension, accompanied by WNW to NW compression (group 1), is inferred between 1.1 and 0.9 Ga (Sveconorwegian). The formed structures were then most likely reactivated during Phanerozoic tectonic events, such as the Caledonian orogeny, but maybe also by the present-day stress field, which is acknowledged by a similar direction of compression (Viola et al. 2009, GFZ 2023).

Both paleostress fields of group 1 and 2 were transpressive in character, where permutations of  $\sigma_1$  and  $\sigma_2$  lead to subordinate extensional paleostress fields.

NE striking faults, which are partly interpreted from geophysical lineament (see previous chapter), were optimally oriented to move either as normal or strike slip (sinistral) under N to NE compression and as reverse or strike slip (dextral) under WNW to NW compression (Figure 5-2).

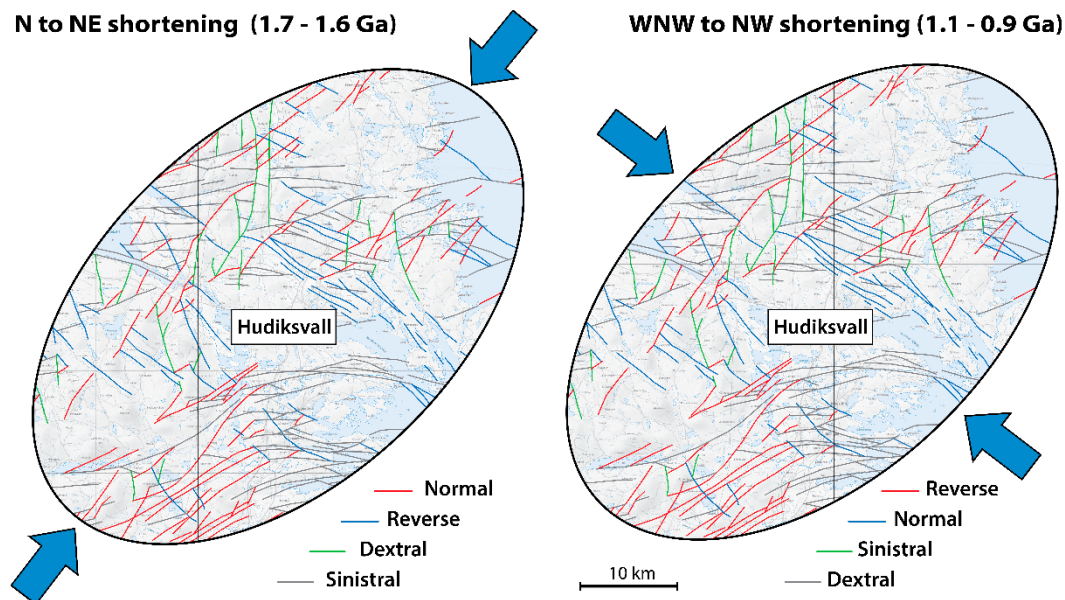


**Figure 5-3.** Interpreted regional paleostress fields as derived from fault-slip data presented in this study. Geophysical lineaments (see Chapter 6) are colored according to their predicted fault kinematics within the stress field. The Hudiksvall earthquake cluster strikes NE parallel to the red lineaments (see also Figure 4-1). Indicated age ranges are solely based on mechanical compatibility with tectonic events mentioned in related studies (e.g., Viola et al. 2009 and Saintot et al. 2011).

## 6 Geophysical modelling

### 6.1 Input data

#### 6.1.1 Airborne geophysics

Airborne geophysical data have been acquired over the project area during 18 campaigns between 1978 and 2015. The nominal flight line separation is 200 m over land and 400 to 1 000 m above the Bothnian Sea. The flight azimuth has varied between north–south and northeast–southwest between the different flight areas. During these nearly 40 years of data collection, systems and sensors have been upgraded with a transition to GPS positioning as well as improved sensitivity and accuracy for all sensors and a denser sampling frequency. Until 1994, the nominal flight altitude was 30 m, but as of 1995 measurements have been carried out at 60 m nominal flight altitude. For measurements of the total magnetic field, which was done during all campaigns, an accuracy of c. 5 nT and a measurement point separation of c. 40 m was achieved in the older campaigns. For campaigns flown after 2007 the accuracy had improved to < 0.3 nT and point separation reduced to about 6 m. This results in a great variation in data quality for the airborne data between different locations in the area.

The magnetic data of the individual surveys were upward continued to the same flight altitude and reduced to the geomagnetic North Pole before merging, to reduce the differences between the data-sets. Some differences remain, however, and can be seen as visible linear artefacts at the boundaries and overlapping areas of the surveys. These features can affect interpretation, but more importantly, even small differences can be amplified in subsequent processing and inverse modelling and affect the modelling results.

A map of the total magnetic field intensity after reduction to the North Pole can be seen in Figure 6-1A. Positive anomalies (red hues) show areas with stronger magnetic properties, which are often linked to ferro- and ferrimagnetic minerals (such as magnetite) in, for example, mafic intrusions or in layers within sedimentary or volcanic formations. Figure 6-1B shows the first vertical derivative of the pole-reduced total magnetic field intensity, which helps to highlight different structures in the magnetic anomaly pattern in the area.

Modern measurements of the electromagnetic field within the VLF band (Very Low Frequency, 15–30 kHz) have been carried out in eight airborne campaigns between 1990 and 2021. In modern VLF measurements, the signal is recorded from two transmitters, providing information on subsurface resistivity that can be used to calculate directionally independent maps of the apparent resistivity and current density. VLF measurements were also carried out before 1990, but the signal from only a single transmitter was recorded. This revealed electrical conductors oriented in the direction of the transmitter, but very low sensitivity to electrical conductors oriented perpendicular to the direction of the transmitter. Aside from the inherent bias in the single frequency VLF sensor, the data in the area with seismic activity southwest of Hudiksvall is of low quality and hence this data does not contribute much useful information for interpretation or modelling. The area covered with modern VLF data is located in the northern and western part of the project area and covers only a small part of the seismically active zone. This data therefore provides very limited knowledge about structures within the seismically active zone, but can contribute with an improved picture of nearby regional structures that are oriented towards, and possibly enter, the active zone.

The apparent resistivity is shown in Figure 6-2. Blue hues indicate low electrical resistivity, that is, good electrical conductivity, which may indicate the presence of, for example, electrically conductive mineralizations or water-bearing formations or structures. However, it can also be the response from lakes, rivers, creeks and infrastructure. A careful follow-up of known bodies of water and infrastructure is necessary before interpretation.

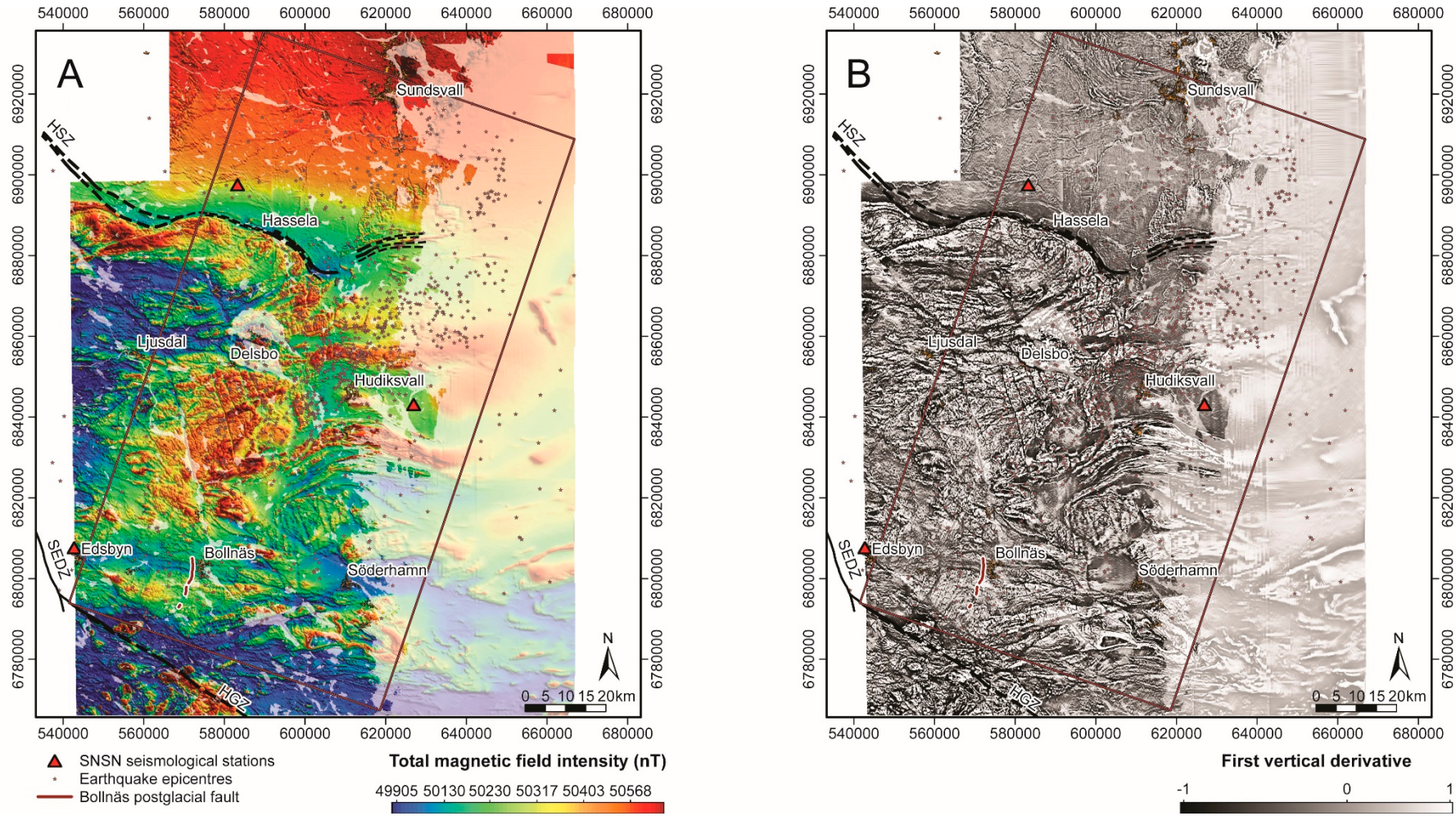


**Figure 6-1.** A) Total magnetic field intensity based on airborne magnetic measurements from 1978 to 2015 after reduction to geomagnetic north pole. B) The first vertical derivative of pole-reduced total magnetic field intensity (shown in A) that emphasizes structures such as deformation zones and regional folds. HSZ = Hassela shear zone; SEDZ = Storsjön–Edsbyn deformation zone; HGZ = Hagsta gneiss zone. Stars mark the epicentres of earthquakes recorded between 2000 and 2018. Brown areas are towns and semi-transparent white areas are water surfaces. The red and black line delimits the extent of the project’s area of interest.

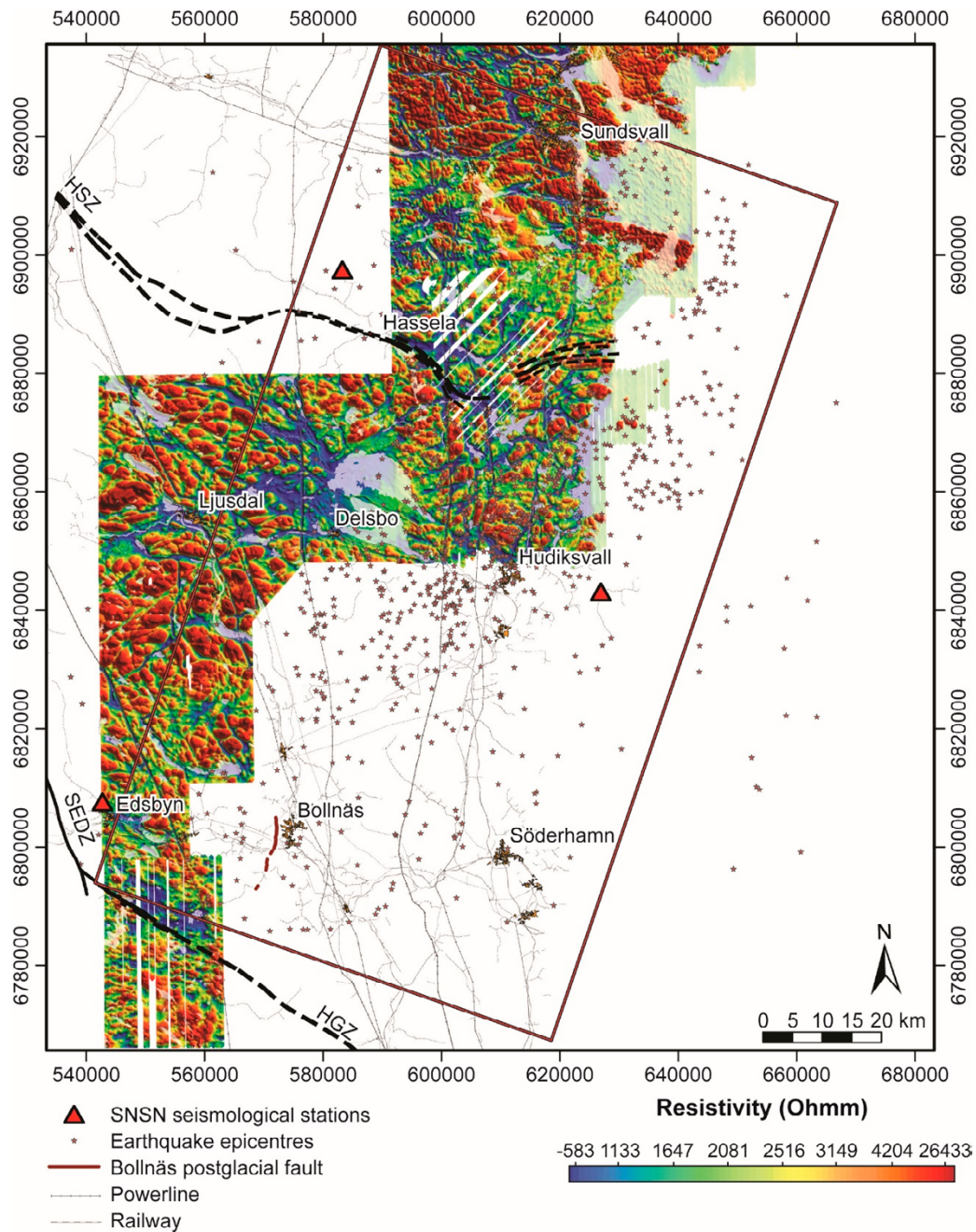


**Figure 6-2.** Apparent resistivity calculated based on the airborne dual frequency VLF measurements carried out between 1990 and 2021. Railways and power lines cause several of the clear linear anomalies that indicate increased electrical conductivity and are therefore included in the figure. HSZ = Hassela shear zone; SEDZ = Storsjön–Edsbyn deformation zone; HGZ = Hagsta gneiss zone. Stars mark the epicentres of earthquakes recorded between 2000 and 2018. Brown areas are towns and semi-transparent white areas are water surfaces. The red and black line delimits the extent of the project’s area of interest.

## 6.1.2 Gravity

Onshore gravity measurements have been carried out in the field by various actors in different campaigns throughout the 1900s and early 2000s. Marine gravity measurements in the Bothnian Sea were carried out in the 1980s and 1990s. Today there is a regional coverage in the area with a point density of less than 0.5 measurement points per km<sup>2</sup>, apart from the areas around Delsbo, Söderhamn and Sundsvall where it reaches at best about 1 measurement point per km<sup>2</sup>.

The gravity anomaly map seen in Figure 6-3 is based on all existing gravity data and has been calculated as the difference between the Bouguer anomaly (fully corrected gravity anomaly) and a 3 km upward-continuation of the Bouguer anomaly. Generally, mafic rocks such as gabbro and diabase, have relatively high density and give rise to positive gravity anomalies that indicate local mass excesses (red hues). Felsic rocks, such as granite, generally have relatively low densities and give rise to negative gravity anomalies or local mass deficits (blue hues). Deformation zones and impact structures, for example, can also give rise to negative gravity anomalies. The sparse measurement point distribution means that the anomalies in the area primarily represent very large-scale geological structures or units.

## 6.1.3 Petrophysics

Petrophysical data are used to link geophysical anomalies with a geological source and to guide modelling of geophysical data. The SGU database of petrophysical data contains measurements of 1 127 petrophysical samples within and in the immediate vicinity of the project area. 245 of these samples lack information about the bedrock and were not included in this study. The distribution of magnetic susceptibility versus density of these samples is shown in Figure 6-4.

The majority of the samples in this area (591 samples) are intrusive and metaintrusive rocks of felsic to intermediate composition with measured density that in general lies between approximately 2 600 and 2 800 kg/m<sup>3</sup> and has an average of 2 671 kg/m<sup>3</sup>. Most of the sedimentary and metasedimentary rocks (58 samples) fall within the same range of measured density and have an average density of 2 703 kg/m<sup>3</sup>. The spread in magnetic susceptibility in these groups is large, ranging between -10 and 96 350  $\mu$ SI (average 4 439  $\mu$ SI) for the felsic to intermediate intrusive and metaintrusive rocks and between 150 and 59 680  $\mu$ SI (average 2 806  $\mu$ SI) for the sedimentary and metasedimentary rocks. These form the bulk of a main group that also include most of the samples of intrusive and volcanic rocks of unspecified composition, as well as pegmatite, fault rocks, and sulphide mineralizations. At low magnetic susceptibility, between 100 and 1 000  $\mu$ SI, there is a trend of increasing density from 2 600 to 3 000 kg/m<sup>3</sup>. This trend is connected to increasing mafic content and metamorphic grade in low-magnetic intrusive and sedimentary rocks as well as a group of samples labelled as other metamorphic rocks (including migmatite, greenstone and amphibolite).

Felsic volcanic rocks have the lowest measured density with an average of 2 566 kg/m<sup>3</sup> but with 15 out of the 18 samples having density between approximately 2 375 and 2 550 kg/m<sup>3</sup>. Samples of intermediate to mafic rocks (26 samples of gabbro and 6 samples of diorite) have measured density that range between 2 677 and 3 164 kg/m<sup>3</sup> (average 3 015 kg/m<sup>3</sup>) and measured magnetic susceptibility that range between 450 and 203 700  $\mu$ SI (average 82 549  $\mu$ SI). The measured density and magnetic susceptibility of diabase (17 samples) fall between 2 948 and 3 109 kg/m<sup>3</sup> (average 3 014 kg/m<sup>3</sup>) and between 9 490 and 92 740  $\mu$ SI (average 26 550  $\mu$ SI), respectively. Other rock samples classified as having a mafic or ultramafic composition (23 samples) have measured density in the range 2 770–3 279 kg/m<sup>3</sup> (average 3 026 kg/m<sup>3</sup>) and magnetic susceptibility in the range 59–309 100  $\mu$ SI (average 40 433  $\mu$ SI). Thus, the samples classified as intermediate to mafic have a large spread in both density and magnetic susceptibility but in general have high density and magnetic susceptibility compared to the other rock types.

There are also 29 samples in the database taken from the vicinity of the Gruvberget mine, north of lake Dellen, that do not have a specified bedrock type. The main commodities extracted from the Gruvberget mine were iron, titanium and vanadium hosted in mafic intrusions. The Gruvberget samples have a measured density and magnetic susceptibility ranging between 2 789 and 4 055 kg/m<sup>3</sup> (average 3 207 kg/m<sup>3</sup>) and 877 and 2 046,000  $\mu$ SI (average 401 335  $\mu$ SI), respectively.

The 26 samples of supracrustal rocks of unspecified composition show a wide range of values in both density and magnetic susceptibility. Most of the 245 samples excluded due to lack of information about the bedrock type have petrophysical properties that are comparable with the main groups of felsic-intermediate intrusive rocks, sedimentary rocks, metamorphic rocks and felsic volcanic rocks.

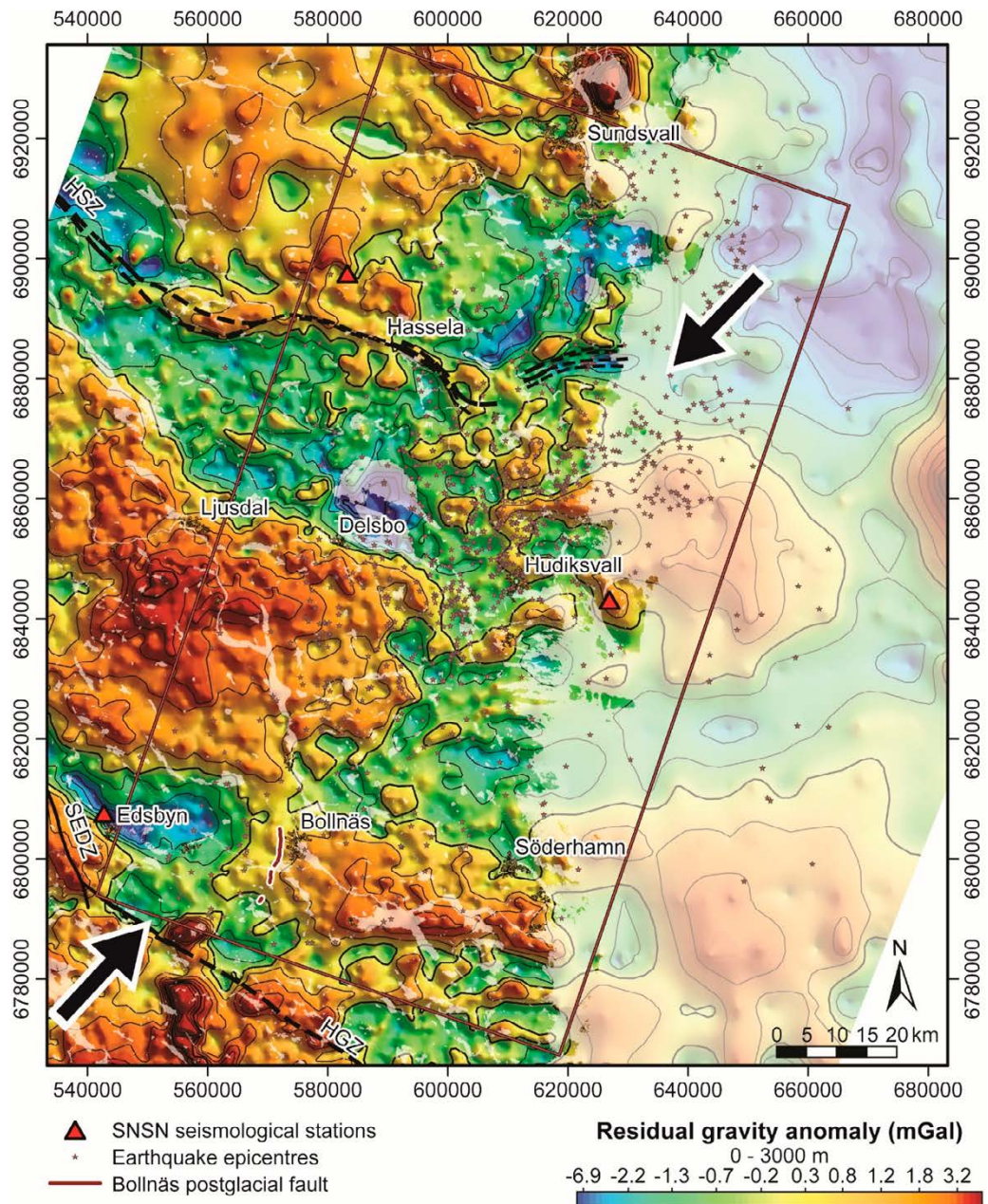


**Figure 6-3.** Gravity anomaly map based on gravity measurements collected up until 2020, calculated as the difference between the Bouguer anomaly and a 3 km upward continuation of the same. The two arrows highlight a possible large-scale lineament in the gravity anomaly that is roughly aligned with the seismicity. HSZ = Hassela shear zone; SEDZ = Storsjön–Edsbyn deformation zone; HGZ = Hagsta gneiss zone. Iso-lines outline 5 mGal (thick lines) and 1 mGal (thin lines) equidistance. Stars mark the epicentres of earthquakes recorded between 2000 and 2018. Brown areas are towns and semi-transparent white areas are water surfaces. The red and black rectangle delimits the extent of the project's area of interest.

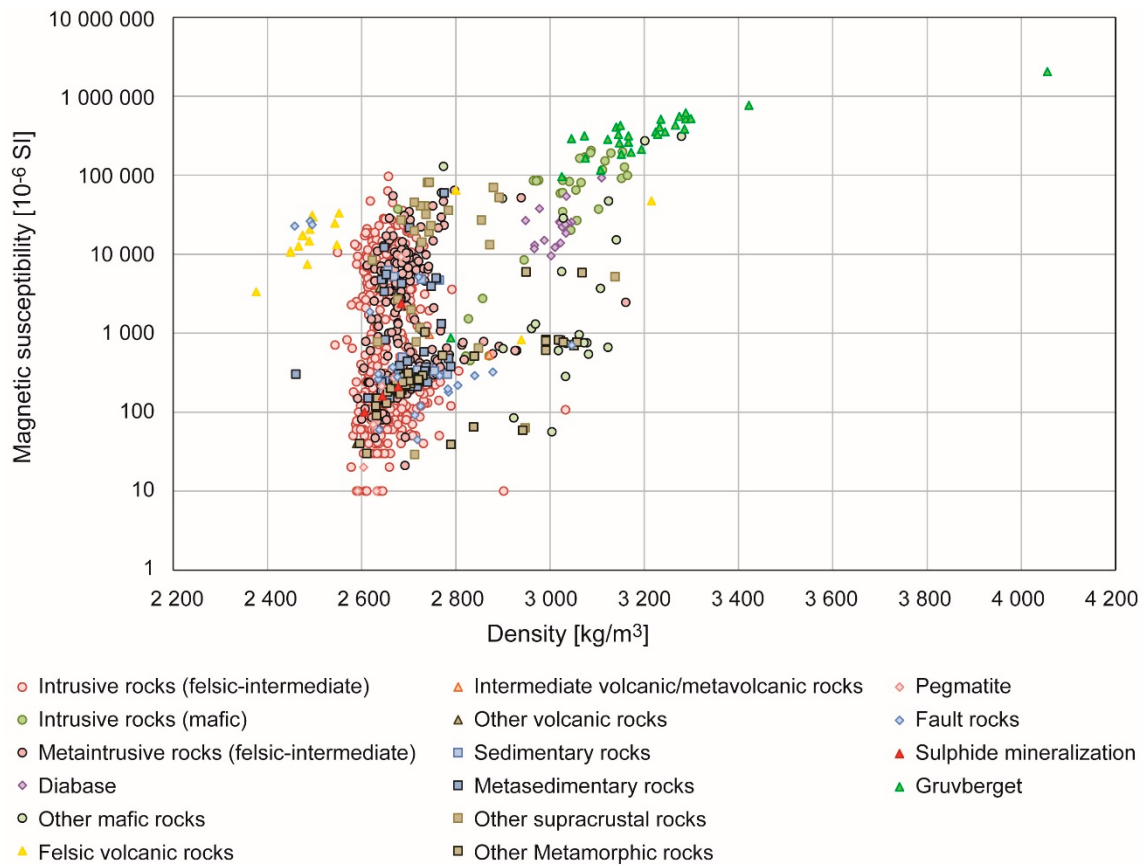


**Figure 6-4.** The distribution of magnetic susceptibility versus density among the 882 petrophysical samples within the area of interest.

## 6.2 Results

### 6.2.1 Interpretation of aeromagnetic data

In 2020, aeromagnetic data from measurements acquired before 2021 were used to interpret magnetic lineaments and connections, as shown in Figure 6-5. Magnetic lineaments (Figure 6-5A), which are linear low-magnetic anomalies (blue hues) or linear breaks in the anomaly pattern, are often linked to deformation zones and indicate the presence of faults, fractures or shear zones. Magnetic connections (Figure 6-5B) trace positive magnetic anomalies (red hues) that may represent and highlight, for example, dike intrusions or fold patterns of layered sedimentary or volcanic formations.

The Hassela shear zone (HSZ) is a clear boundary between the northern Bothnia-Skellefteå lithotectonic unit and the Ljusdal lithotectonic unit to the south. Few magnetic lineaments can be distinguished north of the HSZ (Figure 6-5). Magnetic connections can be linked to possible variation in metasedimentary rocks just west of Sundsvall, as well as both subvertical dikes with a north to northeast direction (e.g., northeast of Hassela) and subhorizontally lying diabase intrusions (e.g., east of Hassela).

In the Ljusdal lithotectonic unit, south of HSZ, the bedrock shows a greater variation in magnetic properties (Figure 6-1) and much more structures can be distinguished. The impact structure north of Delsbo is clearly seen as a circular structure with stronger magnetic properties than its surroundings.

In the western part of the Ljusdal lithotectonic unit, from Delsbo-Bollnäs and westwards, a large number of magnetic lineaments are observed that indicate local to regional deformation zones that cut through the granitic to granodioritic plutonic rocks with little sign of regional plastic deformation in the magnetic data. Two major deformation zones branch off from the HSZ towards west–southwest (Figures 2-1 and 6-1). The easternmost of these passes north of Delsbo and further on past Ljusdal. This zone separates a mostly low-magnetic bedrock with several east–west oriented anomalies north of Ljusdal, from a bedrock with a largely high-magnetic and more homogenous anomaly pattern on its southeastern side. Several major deformation zones can be followed in a south–easterly to south–south–easterly direction throughout this western area, for example just east of Ljusdal in the direction towards Bollnäs. Between Ljusdal and Edsbyn a few magnetic anomalies that are relatively strong for this area appear to be linked to local mafic intrusions.

In the area east of Delsbo-Bollnäs and out into the Bothnian Sea, more regional plastic deformation and large-scale folding is observed in the metasedimentary packages that form part of the bedrock here. Several south–southwest oriented lineaments (red in Figure 6-5A) are seen as breaks in the folded anomaly pattern in this area, especially over land north and west of Hudiksvall where they appear to be parallel with the perceived direction of the seismically active zone. South–east oriented lineaments are also abundant. The lower resolution of airborne magnetic data over the Bothnian Sea does not allow for the details of these structures to be followed further off-coast. It is possible that the regional folding is also present further west but is not seen as clearly in the magnetic response of the more homogeneous plutonic rocks that dominate there.

The major Storsjön-Edsbyn deformation zone (SEDZ) enters the map area from the northwest, just west of Edsbyn, and connects with the more east–south–east oriented Hagsta gneiss zone (HGZ) that separates the Ljusdal lithotectonic unit from the Bergslagen lithotectonic unit to the south. However, a network of larger deformation zones in a slightly more east–west direction than the Hagsta gneiss zone can be seen along the southernmost parts of the project area, north of HGZ, marking the southernmost extent of the rocks with clear regional folding (see “Söderhamn zone” in Chapter 7).

The link between aeromagnetic lineaments and the seismicity is unclear. The seismic activity registered prior to this project suffers from uncertainties in locating earthquake hypocentres and shows a significant spread geographically. No clear structure has currently been identified in the magnetic data that can be directly linked to the seismic activity registered before the start of the project. The majority of the earthquakes in the seismically active zone between Hudiksvall and Delsbo, have been located to the regionally folded eastern part of the Ljusdal lithotectonic unit. The earthquake cluster appears to lie in a diffuse elongated area (marked as grey in Figure 6-5) that includes the fold hinges (red-to-blue lines in Figure 6-5B) and the western extent of folding, a large number of south–southwest oriented lineaments (red lines in Figure 6-5A) that break the folding pattern, and small low-magnetic areas where lineaments are not distinguishable above the noise in the aeromagnetic data. Several of the south–southwest oriented lineaments in this zone could represent faults that may be involved in the observed seismicity and may be of interest for further investigation. The known Bollnäs postglacial fault (Smith et al. 2014) partially aligns with some of these south–southwest oriented lineaments just southwest of the town of Bollnäs. New information on local earthquakes, and in particular a better localization of their hypocentres, together with updated knowledge of bedrock geology, structures and kinematics may possibly show whether some of these structures can be more clearly linked to the observed seismicity.

Magnetic lineaments and connections are used for modelling and as part of the background material for updating the SGU bedrock geological model (SGU 2021b), which is done continuously throughout the project.

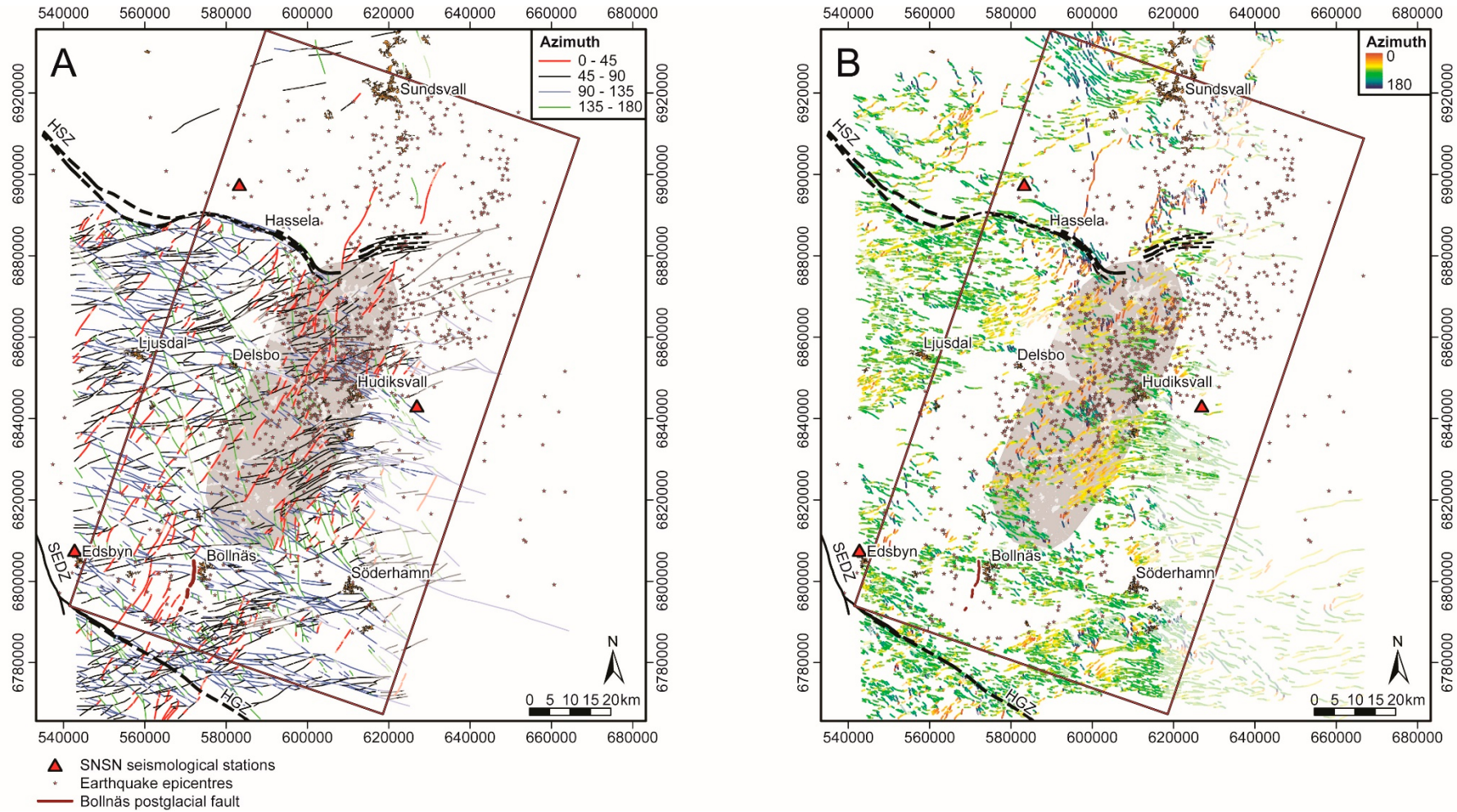


**Figure 6-5.** Interpretation of magnetic lineaments (A) and connections (B) based on data from aeromagnetic measurements collected between 1978 and 2015 (see Figure 6-1). The grey area is defined on the basis of the interpretation of the aeromagnetic data (folding pattern, lineaments, lithological boundaries) in relation to the distribution of the observed seismicity. HSZ = Hassela shear zone; SEDZ = Storsjön–Edsbyn deformation zone; HGZ = Hagsta gneiss zone. Stars mark the epicentres of earthquakes recorded between 2000 and 2018. Brown areas are towns and the red and black rectangle delimits the extent of the project's area of interest.

## 6.2.2 Interpretation of gravity data

Several of the large-scale structures, such as the impact structure at Delsbo, HSZ, SEDZ and large-scale possibly lithological boundaries within the Ljusdal lithotectonic unit, are observed in gravity data (Figure 6-3) and show good correlation with the aeromagnetic data at this regional scale (Figure 6-1). The sparsity of the data is however large and gives much uncertainty in interpreting local features in the gravity data. The gravity anomaly indicates higher density in the western plutonic rocks of the Ljusdal lithotectonic unit between Ljusdal and Edsbyn and lower density in the eastern parts, between Bollnäs, Söderhamn and Hudiksvall, where regionally folded metasedimentary rocks occur. A possible large-scale lineament, or set of subparallel lineaments, can be perceived at the boundary between these two areas, passing between Hudiksvall and Delsbo in the south–south–west direction towards Bollnäs, as indicated by the two arrows in Figure 6-3. This possible large-scale boundary or zone is roughly parallel and partly collocated with the earthquake cluster and correlates with the aforementioned diffuse zone interpreted on the basis of the anomaly pattern in aeromagnetic data where several south–south–west oriented magnetic lineaments are observed.

## 6.2.3 3D geophysical modelling

Inverse modelling of geophysical data is a numerically iterative procedure of finding a subsurface model that satisfies the measured geophysical data within a certain error-threshold. Geophysical data suffer from limitations in resolution which results in issues with ambiguity and an infinite number of subsurface models that can satisfy observed data. Therefore, aside from high-quality data, inverse modelling also requires various regularizations and constraints, to be able to resolve a geologically viable model. Some of these are mathematical in nature, e.g. model geometry and resolution, smoothness, required accuracy etc. Other important constraints to limit the number of possible solutions are based on a-priori information mainly connected to the geology, such as the geometry of known geological formations and structures, and maximum and minimum bounds of physical properties. With respect to the latter, high-quality and statistically sound petrophysical data is vital. Petrophysics include a broad range of bedrock types and a large span of petrophysical properties. To exclude model results with unrealistic petrophysical properties, densities are constrained to range between 2400 and 4000 kg/m<sup>3</sup> and magnetic susceptibilities to between 10<sup>-6</sup> and 1 SI.

Aeromagnetic data and surface gravity data were inverted independently, and constrained by petrophysical results, using the VOXI 3D inversion extension in Geosoft Oasis Montaj (Seequent, 2022) to produce smooth models of the subsurface distribution of density and magnetic susceptibility, respectively. The VOXI subscription is restricted to voxel models having maximum 250 × 250 cells in the x and y direction, which in turn limits the resolution and the size of the area. Because the area of interest is large, the area was split into several overlapping patches, *i1–i6*, of different sizes that were used to define the lateral extent of inversion models. The largest of these (*i1* in Figure 6-6) covers a rectangular area of 55.5 × 70 km with a cell size of 250 × 250 m while the four smallest patches (*i3–i6* in Figure 6-6) cover square areas of 25 × 25 km with cell sizes of 100 × 100 m. A patch of intermediate size (*i2* in Figure 6-6) has a cell size of 175 × 175 m and covers a rectangular area of 40 × 43 km that encompass the small patches. These areas are shown in Figure 6-6.

Results from inverse modelling of magnetic and gravity data are presented below. All grids, voxel models containing inversion results and generated iso-surfaces were exported and provided for subsequent geological modelling and interpretation.

Inversion of aeromagnetic data would benefit from reacquisition of a more uniform dataset with fewer boundaries and differences in different survey parameters. A larger areal coverage of modern airborne VLF data, similarly acquired with fewer differences in survey parameters, would allow calculation of directionally independent maps of apparent resistivity as well as inversion to gain knowledge at depth about electrically conductive structures or formations. Inversion of gravity data would greatly benefit from a much denser sampling in the area.

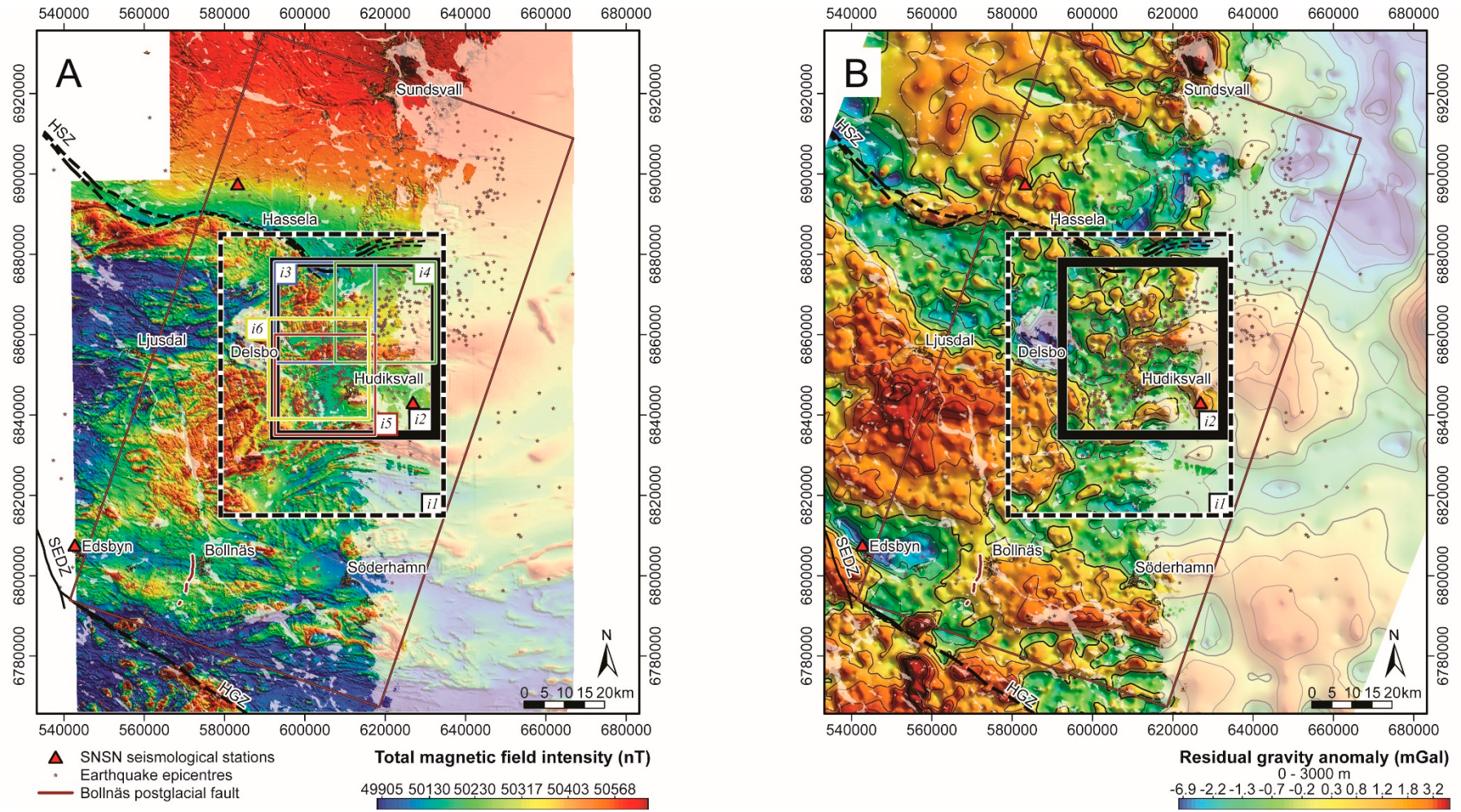


**Figure 6-6.** Areas of interest for inversion, *i1*–*i6*, on the (A) total magnetic field intensity map and (B) gravity anomaly map. HSZ = Hassela shear zone; SEDZ = Storsjön–Edsbyn deformation zone; HGZ = Hagsta gneiss zone. Stars mark the epicentres of earthquakes recorded between 2000 and 2018. Brown areas are towns and semi-transparent white areas are water surfaces. The red and black rectangle delimits the extent of the project's area of interest.

### **Results – 3D inversion of aeromagnetic data**

Inversion of aeromagnetic data was done for all subareas shown in Figure 6-6. Inversion results for two of the smaller patches are seen in Figure 6-7. Two different types of magnetic inversion were used – the first method is a common susceptibility inversion where each voxel in the model is treated as having a scalar susceptibility (Figures 6-7 and 6-8A–D) while the second method is a magnetization vector inversion (MVI) that treats each cell in the model as a 3D vector of the local magnetization (Figure 6-8E–H). The susceptibility inversion is comparatively simple and allows an easy setup of constraints. MVI is insensitive to the direction of magnetic field and the results can give some indication of the magnetization direction, but it is much more complicated to set up constraints since every property of every cell is a vector in 3D. MVI produces a smoother model with less pronounced artefacts but also contains less detail compared to the susceptibility inversion, and both model results can be used complementary in interpretation. The susceptibility model shown in Figure 6-8E–H is the amplitude of susceptibility from magnetization vector inversion without the directional information.

Due to the differences in acquisition between the many airborne surveys, inversion of aeromagnetic data has been done on gridded data – individual surveys were reduced to the geomagnetic North Pole and levelled before being merged to generate the regional grid used for inversion (Figure 6-1A). Even though care has been taken to reduce the acquisition footprint and produce a high-quality grid, artefacts and effects due to these differences are still visible, especially at the boundaries and overlapping regions of the different surveys. These features are treated as real data by the inversion and lead to artefacts in the inversion modelling results. Although several parameters that control the inversion (including model setup and constraints of physical properties and gradients within the model) were adjusted to minimize these effects, they do remain and, in some cases, appear more pronounced than in the original grids. For example, clear east–west-oriented linear features (following certain flight lines) are seen in e.g., Figure 6-7F–H and Figure 6-8B–D. Therefore, great care needs to be taken when interpreting the modelling results.

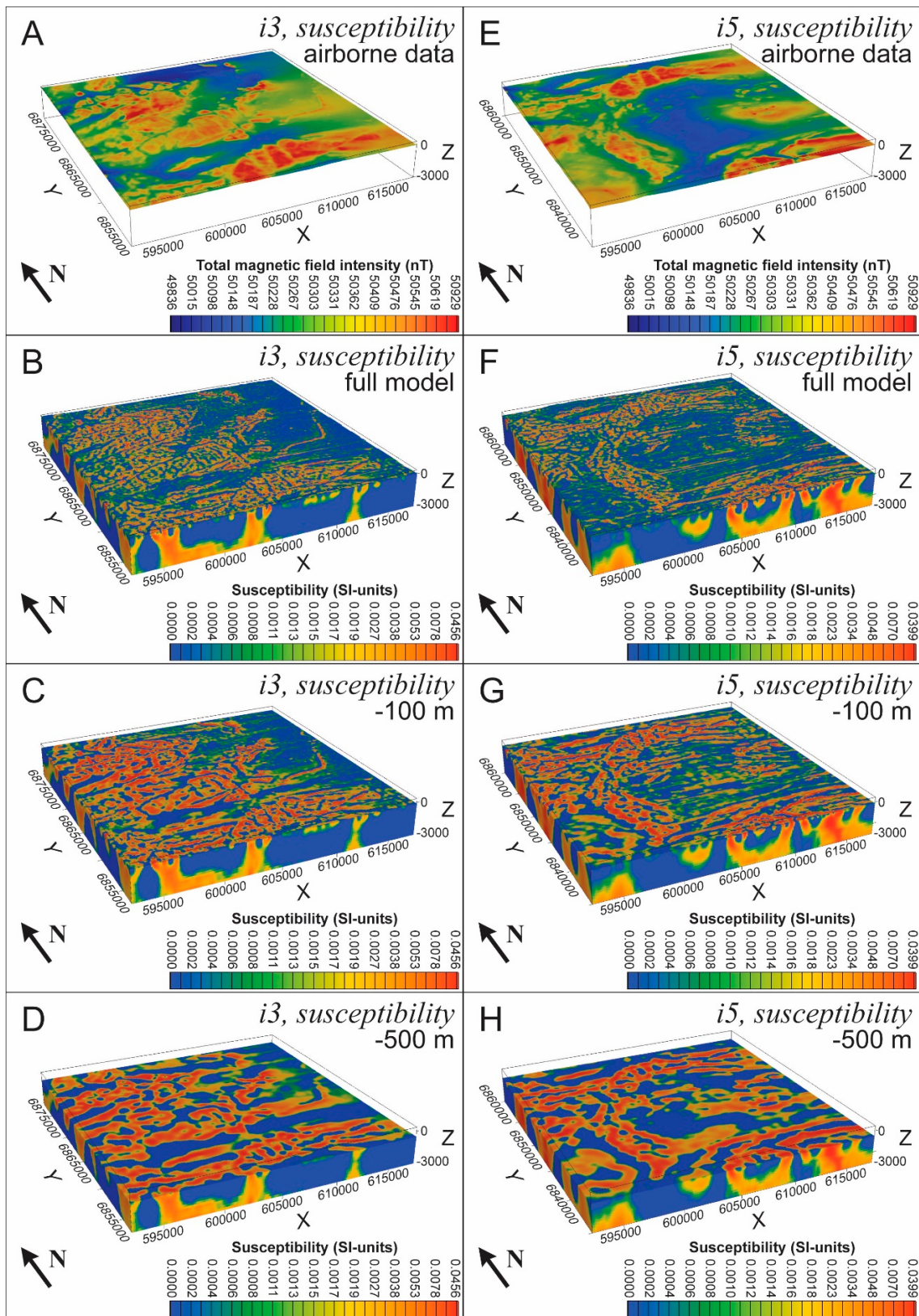


**Figure 6-7.** 3D susceptibility models in the areas i3 and i5 (Figure 6-6) resulting from regular Susceptibility inversion of airborne magnetic data. A) and E) shows the pole-reduced total magnetic field intensity, which is input to the two inversions. B) and F) show the full susceptibility models of i3 and i5, respectively, from the topographic surface to a depth of 3 km below mean sea level. In C) and G) the susceptibility models of i3 and i5, respectively, are sliced at a depth of 100 m below mean sea level and in D) and H) the susceptibility models of i3 and i5, respectively, are sliced at a depth of 500 m below mean sea level. Viewed from SSW.

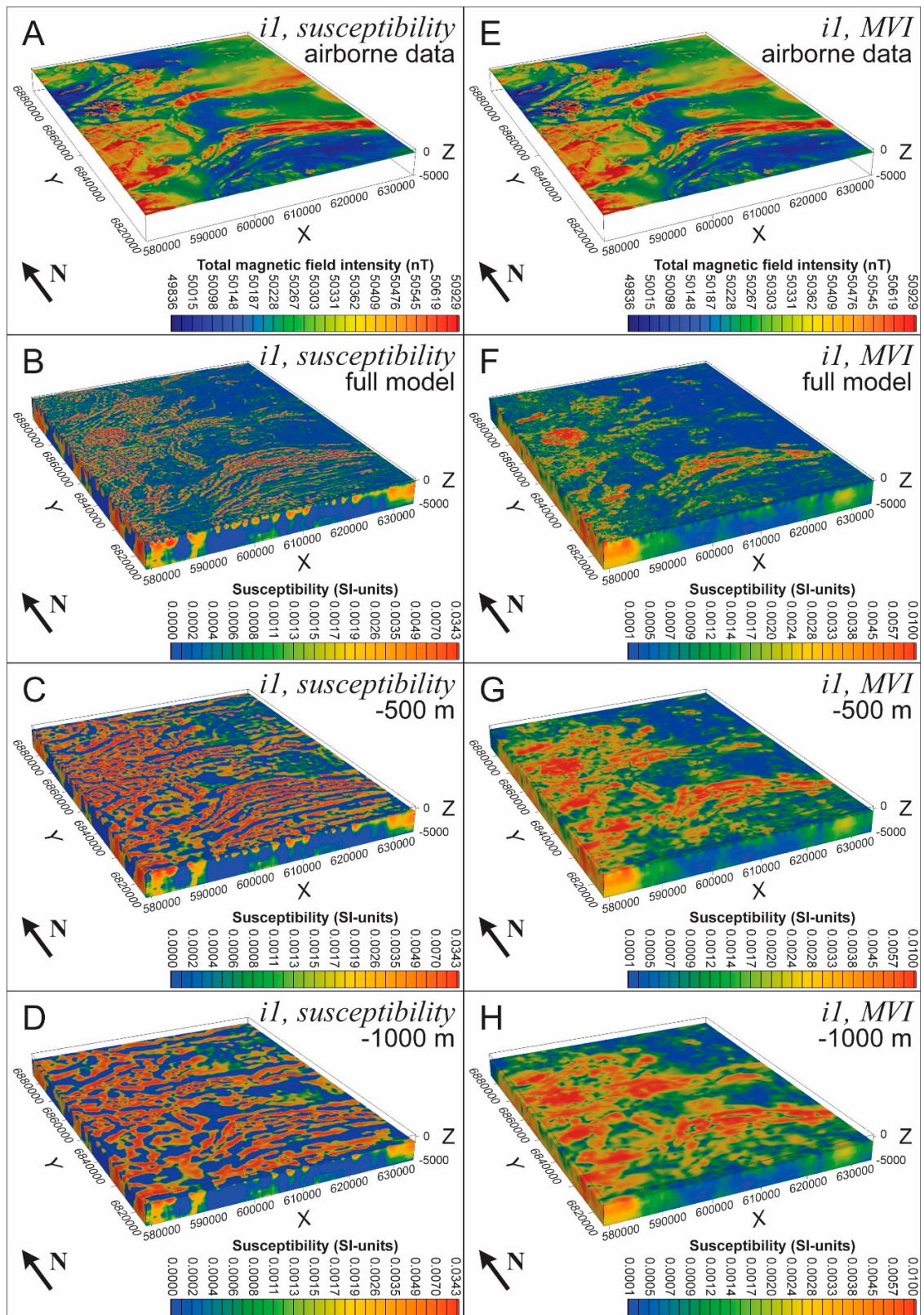


**Figure 6-8.** 3D susceptibility models in the area *i1* (Figure 6-6) resulting from regular Susceptibility inversion (A–D) and magnetization vector inversion, MVI (E–H) of airborne magnetic data. A) and E) shows the pole-reduced total magnetic field intensity, which is input to the two inversions. B) The full susceptibility model, from the topographic surface to a depth of 5 km below mean sea level. In C) and D) the susceptibility model is sliced at a depth of 500 m respectively 1 000 m below mean sea level. F) The full model of the amplitude of susceptibility from MVI, from the topographic surface to a depth of 5 km below mean sea level. In G) and H) a model of the amplitude of susceptibility from MVI is sliced at a depth of 500 m respectively 1 000 m below mean sea level. Viewed from SSW.

Iso-surfaces were generated to delineate different levels of susceptibility in the inversion models. In Figure 6-9, iso-surfaces representing 0.005 SI of the susceptibility inversion results from area *il* are visualized in 3D together with the hypocentres of earthquakes recorded prior to the start of the project (Figure 6-9B). Several prominent northeast–southwest oriented features in the inversion results, seen as susceptibility lows and breaks in susceptibility highs (marked with black lines in Figure 6-9), are more than 10 km long and have depth extents on the order of a kilometre. These are partially coaligned with the interpreted NNE–SSW oriented local magnetic lineaments (Figure 6-5) and parallel with the major linear feature in the gravity anomaly (highlighted by the arrows in Figure 6-3). Their location and orientation also coincides with the seismically active zone around Hudiksvall. These zones appear to project towards the Bollnäs postglacial fault that lies further to the southwest (outside of Figure 6-9, see e.g. Figure 6-1) and have roughly the same orientation. The hypocentres of earthquakes recorded between 2000 and 2018 have very high uncertainty in their location and may have errors of several kilometres. These appear as a cloud of seismicity in 3D (Figure 6-9B) and cannot be linked with any clear structures at depth, but the bulk of them are nevertheless located below the three lineaments highlighted in Figure 6-9A.

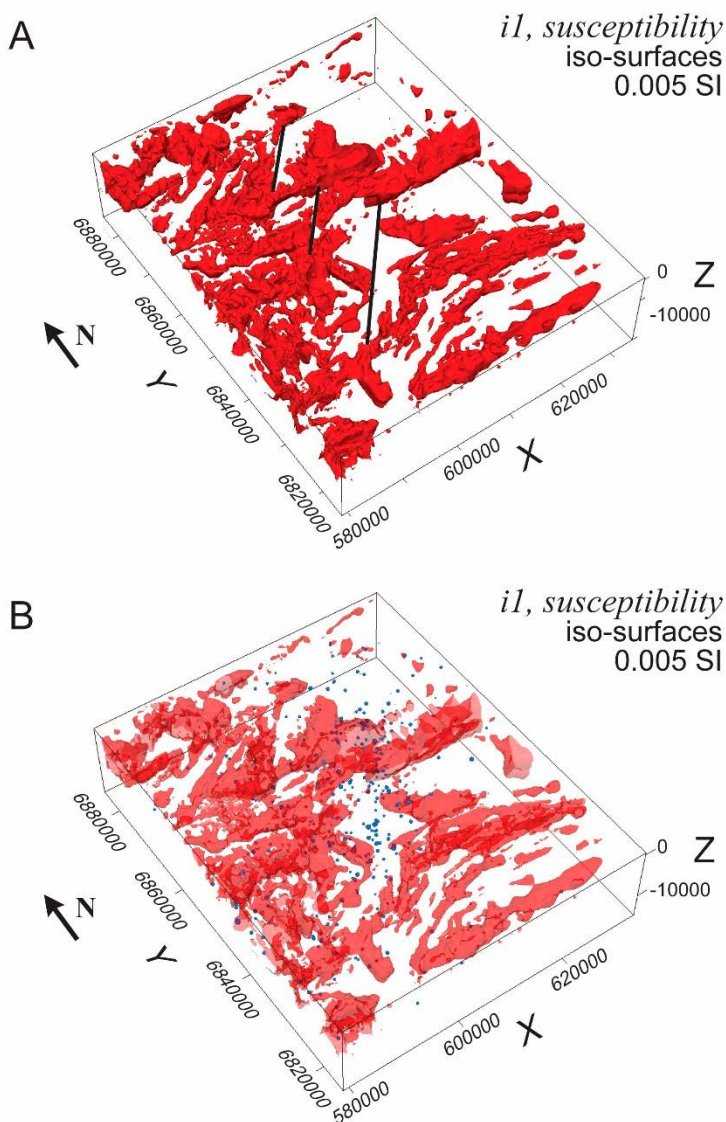


**Figure 6-9.** 3D iso-surfaces delineating regions with susceptibility greater than 0.005 SI based on the 3D susceptibility inversion (see Figure 6-8A–D). The three black lines in A) roughly highlight possible lineaments observed in the inversion results that could be linked with structures parallel with the seismically active zone around Hudiksvall. The blue dots shown together with semi-transparent iso-surfaces in B) are the hypocentres of earthquakes recorded between 2000 and 2018, however the location of these have very high uncertainty. Viewed from SW.

### Results – 3D inversion of gravity data

Inversion of gravity data in this area suffers from very sparse and irregular sampling and the resolution and level of detail is therefore in general low. Because of the low resolution in the gravity data, inversion of this data was only done on the most regional scale, area *i1* in Figure 6-6. Also, in the case of gravity data, inversion was done on gridded data (Bouguer anomaly) to ensure proper sampling to populate all cells in the model. Although the full span in the density of sampled bedrock is quite large, the vast majority of rocks in the area have a density within the narrow band c. 2 600–2 800 kg/m<sup>3</sup>. The inversion is nevertheless constrained to the range 2 400–4 000 kg/m<sup>3</sup>, to include most of the petrophysical samples from the area.

Inversion of gravity data generates a density contrast model showing the deviation from a background density, in this case 2670 kg/m<sup>3</sup> (Figure 6-10). The inversion results in a smooth model with little detail and very small contrast – densities in the model range from c. 2 610 to 2 710 kg/m<sup>3</sup>. Awareness of this is important to avoid overinterpreting this modelling result.

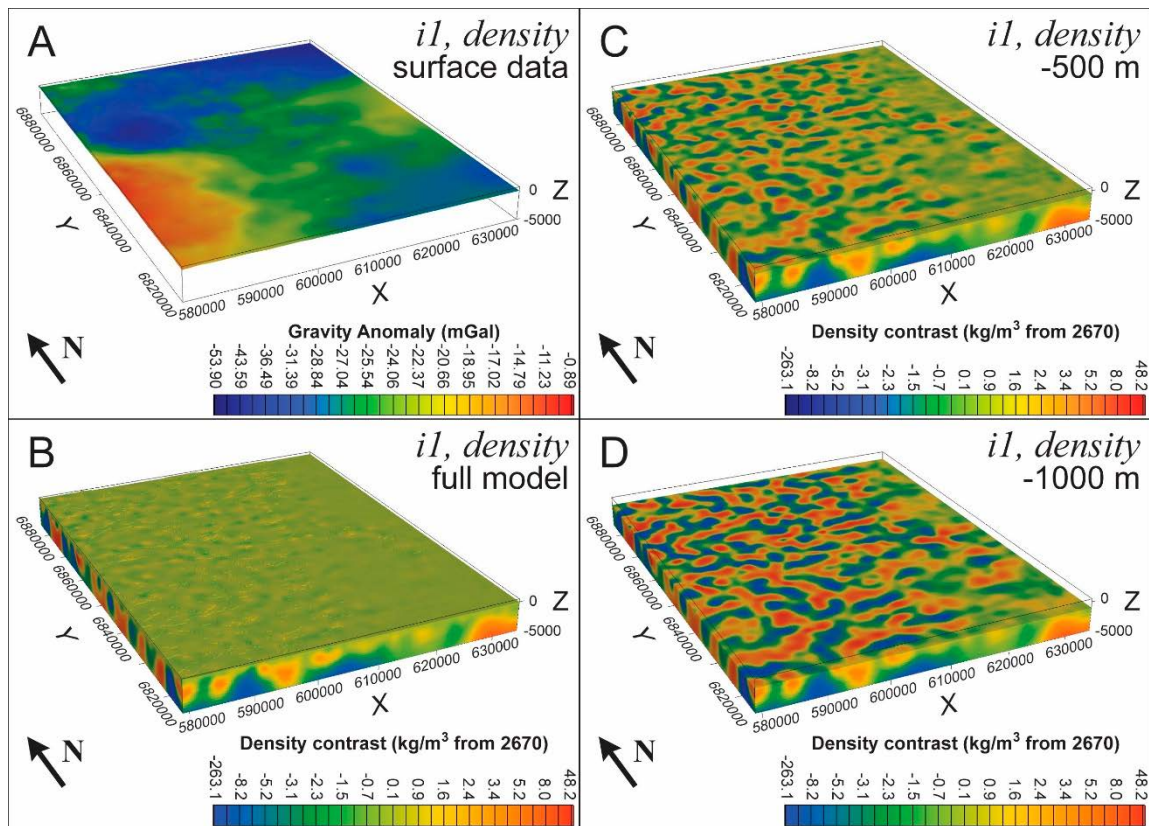


**Figure 6-10.** 3D density model in the area *i1* (Figure 6-6) resulting from inverse modelling of Bouguer anomaly data. A) Bouguer gravity anomaly from surface measurements which is input to the inversion. B) The full density model, from the topographic surface to a depth of 5 km below mean sea level. In C) and D) the density model sliced at a depth of 500 m respectively 1 000 m below mean sea level. Viewed from SSW.



## 7 3D geological modelling

### 7.1 Crustal model of the Ljusdal lithotectonic unit

A three-dimensional crustal model has been created with a lateral extent that includes the vast majority of earthquakes recorded around Hudiksvall between 2000 and 2018. It also covers the entire Ljusdal lithotectonic unit, the southernmost part of the Bothnia-Skellefteå lithotectonic unit and the northernmost part of the Bergslagen lithotectonic unit. The model is created in Leapfrog Geo v. 2023.2 and contains the whole crust and uppermost mantle down to 65 km depth. Modelling results are based on regional-scale geophysical and geological interpretations presented in earlier studies (see paragraph 7.1.1). A revised interpretation of the offshore seismic data and its resulting three-dimensional “alternative crustal model” is presented in Chapter 8.

#### 7.1.1 Input data, methods used and resulting crustal model

A simple, three-layer crustal model was constructed using the offshore reflection seismic lines BABEL line 1, BABEL line 6 and BABEL line C (BABEL Working Group 1990, 1993, which were all recently reprocessed by Buntin et al. (2019). Our interpretations on the upper, middle, and lower crustal boundaries are largely based on Korja and Heikkinen (2005) (Figure 7-1). In general, the upper crust is weakly reflective whereas the lower to middle crust is highly reflective on all profiles. The exact boundaries are, however, somewhat ambiguous considering the fact that seismic reflectivity varies gradually not only with depth but also laterally. Other prominent features that were recognized by Korja and Heikkinen (2005) are the distinct but locally gradual Moho boundary at a depth varying between 45 and 57 km (see also Heikkinen and Luosto 1992, Matthews et al. 1992), a large, weakly reflective, homogeneous unit in the middle of the profiles interpreted as “mafic nucleus” and local strong reflections within the weakly reflective upper crust representing diabase sills (BABEL Working Group 1993, Korja et al. 2001, Buntin et al. 2019, 2021, Buntin and Malhemir, 2021).

Onshore, to the west of the BABEL lines, a 2D crustal layering is based on interpretations from the UPPLAND refraction profile, which was acquired in 2017 and is presented as a series of P-wave and S-wave velocity models in Buntin (2021) (Figure 7-1).

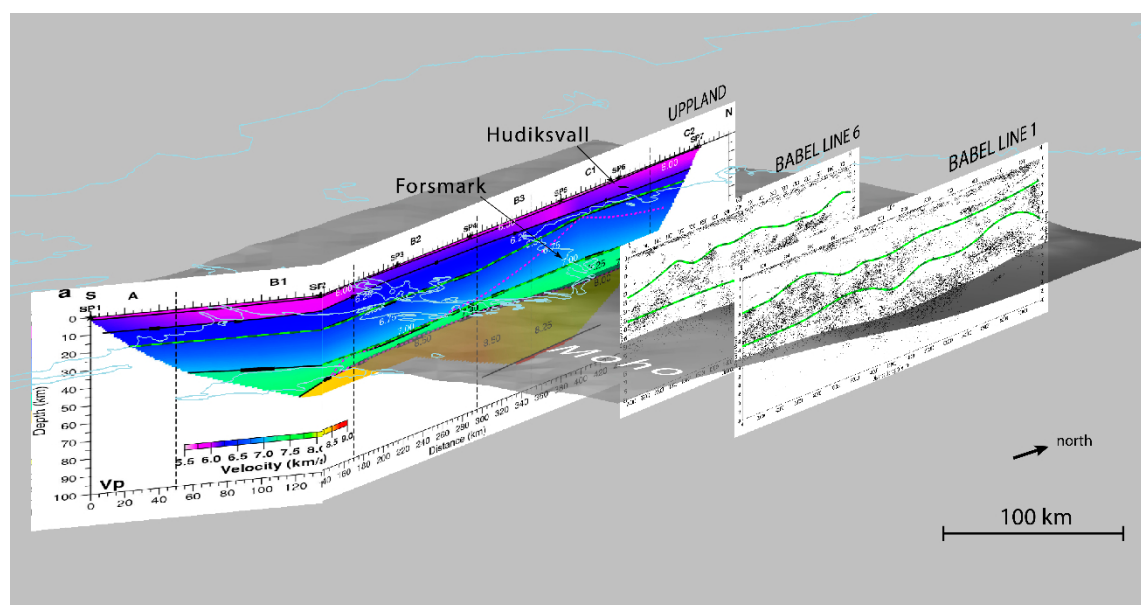


**Figure 7-1.** The reprocessed BABEL seismic reflection line 1 (right) and line 6 (middle) and UPPLAND P-wave velocity refraction line (left) after Buntin et al. (2021). Green dashed lines are our interpretations separating upper, middle, and lower crust. Dark semi-transparent surface represents Moho after Grad et al. (2009). Thin blue line indicates shorelines of Sweden. View is to the northwest in Leapfrog Geo v. 2023.2.

In Leapfrog Geo, the interpreted boundaries parting upper-, middle- and lower crust on each profile were “connected” by triangulated meshes and the evolving volumes were color-filled giving rise to the 3D crustal model (Figure 7-2). The deepest contact surface is represented by the seismic Moho – the crust-mantle boundary – and is directly after Grad et al. (2009).

Subsequently, several southeast-dipping deformation zones or “detachments” were interpreted on the seismic reflection lines Babel 1, 6 and C (Figure 7-3). These interpretations are very similar to earlier interpretations after Korja and Heikkinen albeit with some minor revision. As such, we have extended the deformation zones vertically towards the surface as well as further downwards reaching the lower crust at low angles. Next, the interpreted deformation zones on each profile (BABEL, 1, 6, C) were interlinked and surfaces were modelled in between. The resulting “fault surfaces” or meshes could then also be correlated to the major deformation zones shown on the bedrock map of Sweden at 1:1 million, such as with the Hagsta gneiss zone, the Lindön shear zone and a nameless shear zone directly south of Söderhamn, which we refer to as “Söderhamn zone”. In the north we connect the map trace of the Hassela shear zone with the southward dipping reflectors appearing in the centre of BABEL lines 6 and 1. Further north, in the Bothnia-Skellefteå lithotectonic unit, the connections between mapped shear zones and inferred shear zones at depth becomes uncertain. We do interpret here northwest dipping shear zones from reflectors seen both on BABEL line 1 and line 6, but the surface expression, based on the bedrock map of Sweden at 1:1 million, remains unclear (see Chapter 8). It should be emphasised that the dip of all modelled fault surfaces is solely constrained by the interpreted fault lines on the BABEL lines. The somewhat steeper deep of some faults in the onshore part, such as the Hassela shear zone, is directly caused by the geometry of its map trace.

Finally, the created fault surfaces were used to produce a crustal-scale fault block model for the Ljusdal lithotectonic unit where all major shear zones root into the lower crust (Figure 7-4).

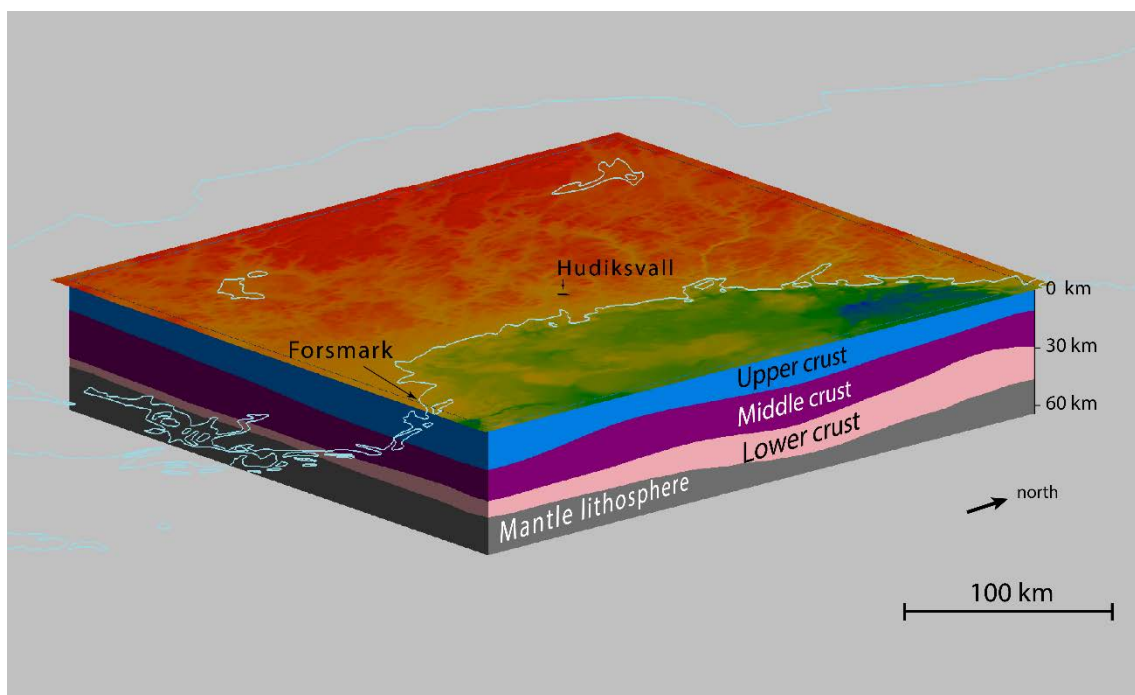


**Figure 7-2.** 3D crustal model consisting of upper crust (blue), middle crust (purple) and lower crust (pink), and upper part of the mantle lithosphere (grey). Surfaces were constructed from 2D interpretations on the seismic profiles BABEL lines 1 and line 6, and UPPLAND 2D seismic velocity model as well as from the Moho depths after Grad et al. (2009) (see Figure 7-1). Notice the relative thick crust in the model’s central part. Overlaying raster compiles topography (red is high) and bathymetry (blue is low). Thin blue line indicates shorelines in Sweden. View is to the northwest in Leapfrog Geo v. 2023.2.

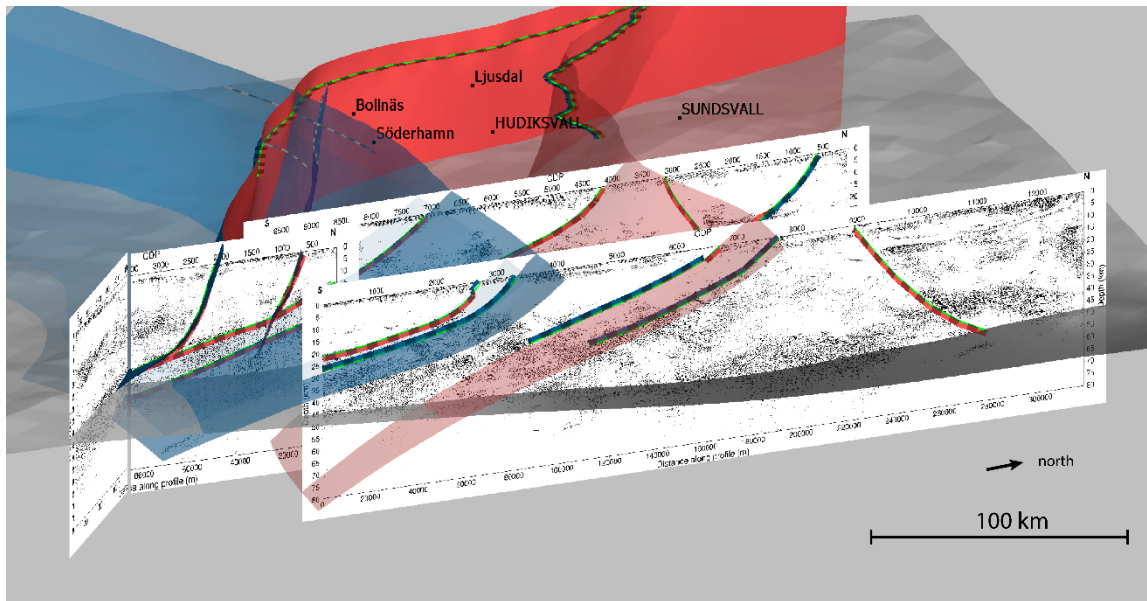


**Figure 7-3.** Crustal-scale shear zones interpreted in this study from reprocessed BABEL lines 1, 6 and C and map traces as displayed on the bedrock map of Sweden at 1:1 million (dashed lines). The resulting “fault” surfaces (meshes) were created by assigning geometric constraints to the individual lines and corresponding map trace. No surface was created here connecting the north-dipping lines in the north (right) because no corresponding map trace is present on the 1:1 million geological map. This surface is, however, displayed in Figure 8-2. The blue and red colors indicate polarity but have no further meaning. Dark semi-transparent mesh (surface) represents Moho after Grad et al. (2009). View is to the west in Leapfrog Geo v. 2023.2.

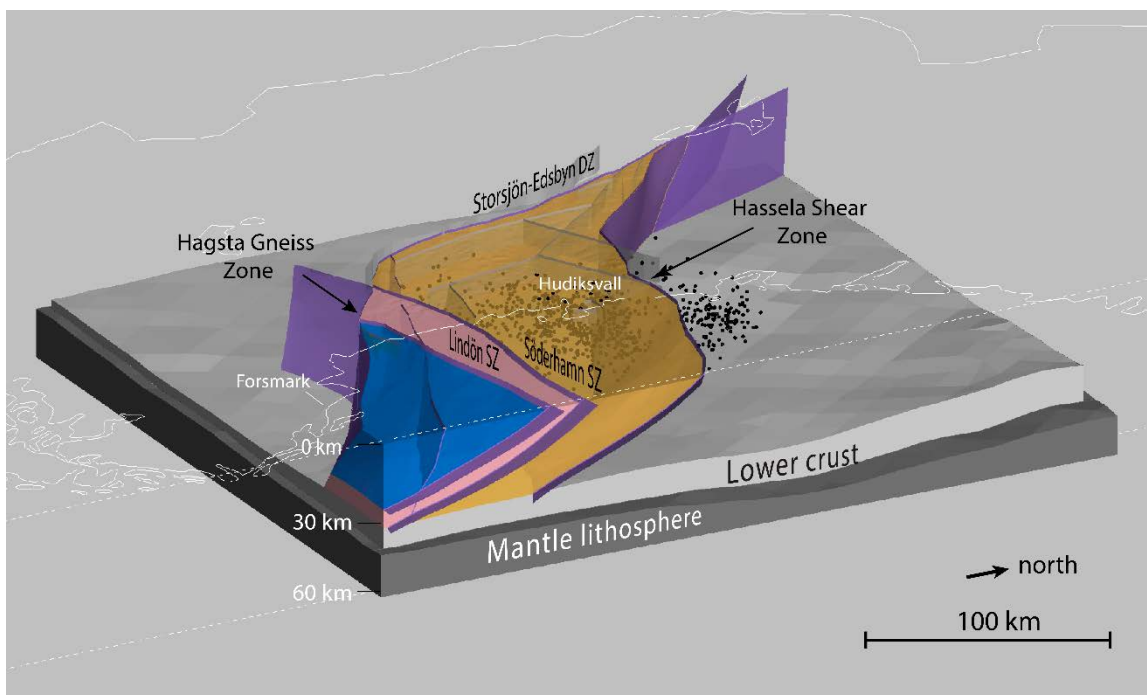


**Figure 7-4.** Fault block model of the Ljusdal lithotectonic unit constrained by the interpreted crustal-shear zones displayed in Figure 7-3. The fault zones are clipped by, and root in, the lower crust (light grey). Bright colors indicate the individual fault blocks and have no lithological meaning. Dark grey volume represents the upper part of the mantle lithosphere as shown in Figure 7-2. Dark point cloud represents the Hudiksvall earthquake cluster recorded between 2000 and 2018. Additional minor faults in grey are from the bedrock map of Sweden 1:1 million and modelled as vertically dipping surfaces. Thin white line indicates shorelines of Sweden. Dashed white line is section line for visualization. View is to the west in Leapfrog Geo v. 2023.2.

## 7.2 Lithology model of the Hudiksvall area

The crustal model presented in the previous paragraph was at first constrained by interpreted lines derived from seismic sections at a certain depth, which were then linked to fault traces at the surface. The construction of the lithology model, on the other hand, builds heavily on the lithologic boundaries as displayed on the bedrock map of Sweden at 1:1 million (SGU 2021a), and is only weakly constrained at depth. The depth extent of the presented lithology model is therefore limited to 5 km below the surface, hence to upper crustal levels. The model's lateral extent captures the Hudiksvall earthquake cluster and its surroundings including most of the Ljusdal lithotectonic unit and the southernmost part of the Bothnia-Skellefteå lithotectonic unit up to Sundsvall.

### 7.2.1 Input data, methods used and resulting lithology model

The resulting lithology model of the Hudiksvall area is presented in Figure 7-5. At the surface, the model is in harmony with the bedrock map of Sweden at 1:1 million.

To prepare for the modelling, the lithological boundaries were extracted per lithology-type from the SGU bedrock database as dxf files using ArcGIS software from ESRI. The dxf files were imported into Leapfrog Geo v. 2022.1 as "GIS-lines", which were then draped onto the topography of the study area to set the elevation for each line. Next, the GIS-lines were transformed into 3D-polylines with the ribbons set to horizontal, ready to be used as input for geological modelling.

When a geological model is first created in Leapfrog Geo, it is a single volume of lithology "Unknown". This Unknown volume is then divided into known lithologies by creating contact surfaces. The type of contact surface that has been used for this exercise is the Intrusion-type contact surface, which removes the existing Unknown lithology and replaces it with the intrusive lithology on the inner side of the contact surface. In the Hudiksvall study area, the dominating lithology is the brownish/pinkish colored metamorphosed granitoids (the 1.87–1.83 Ga Ljusdal batholith). Consequently, we assigned that lithology the role of the "Unknown" and fill the initial 3D model space with that lithology. We then continued by modelling the other lithologies as "intrusions", such as the migmatites/paragneisses mapped in blueish, which then replaced the granitoids locally. Although the migmatites may be older, they geometrically appear to intrude into the granitoids for this modelling exercise.

Following the above recipe, a first-order model was produced by modelling all the lithological boundaries, except the Ljusdal batholith granitoids and offshore sedimentary cover rocks, as "intrusions" with a surface resolution of 400 (unitless). The resulting lithological boundaries of this first-order model are unrealistically spherical at depth, so called "ballooning". We therefore remodelled the lithological boundaries by importing structural measurements (e.g. bedding and foliation) from the SGU database and used those to model a "structural trend" in Leapfrog, which was then used to better constrain the geometry of the intrusion-type contact surfaces at depth.

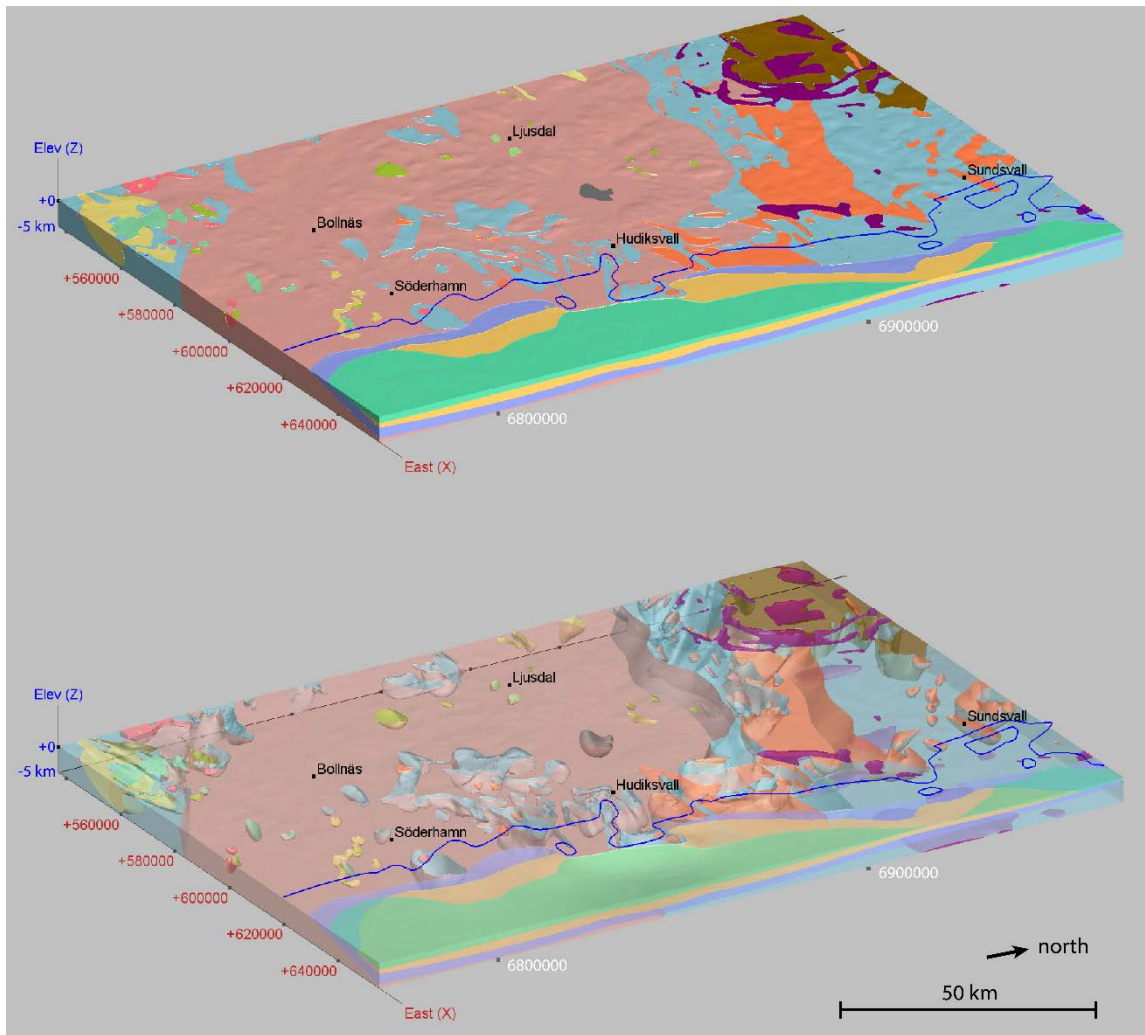


**Figure 7-5.** Lithology model of the Hudiksvall area displayed as solid (top) and semi-transparent (bottom). The model is in harmony with the bedrock map of Sweden at 1:1 million (SGU 2021a) (see Figure 2-1). The modelled lithological boundaries are modelled as “intrusion-type” in Leapfrog Geo v. 2023.2 and constrained by the 2D map traces and planar structural data (see Figure 7-8). The thickness of the offshore sedimentary cover rocks is only poorly constrained by extrapolation of uncertain interpretations on BABEL seismic lines 1 and 6. Also the diabase is modelled mostly conceptually as sills, mimicking the interpretations on BABEL line 1 and 6 after Buntin et al. (2019). Blue line indicates the shoreline of Sweden. View is to the northwest in Leapfrog Geo v. 2023.2.

### Modelling lithological boundaries by applying a structural trend

To remodel the intrusion-type contact surfaces using structural measurements, we extracted strike-dip measurements from the SGU database (SGU 2023) including the planar structure-types bedding ( $n = 86$ ), foliations ( $n = 6\ 125$ ), banding ( $n = 58$ ), gneissosity ( $n = 604$ ) and schistosity ( $n = 837$ ). Even trend and plunge measurements on linear structures were extracted and include stretching- and mineral lineations ( $n = 1\ 153$ ) as well as fold axis ( $n = 216$ ). All structural measurements are from within the Ljusdal lithotectonic unit plus 5 km across its border.

Importing the structural data into Leapfrog Geo v. 2023.2, the planar structures were lumped together ( $n = 7\ 714$ ) and used to extract “form interpolants” from (Figure 7-6A, B). Form interpolants are radial basis function (RBF) interpolants that use planar structural data to control the RBF gradient and can be considered as the modelled 3D equivalent of 2D form lines often seen on maps. The interpolants are typically used for visualising structural data and revealing regional structural patterns in 3D. Technically, the method produces smooth surfaces from irregularly-spaced sparse data. Due to the high “smoothness” of the produced surfaces, the technique is less well suited when large changes in the data values occur within a very short distance.

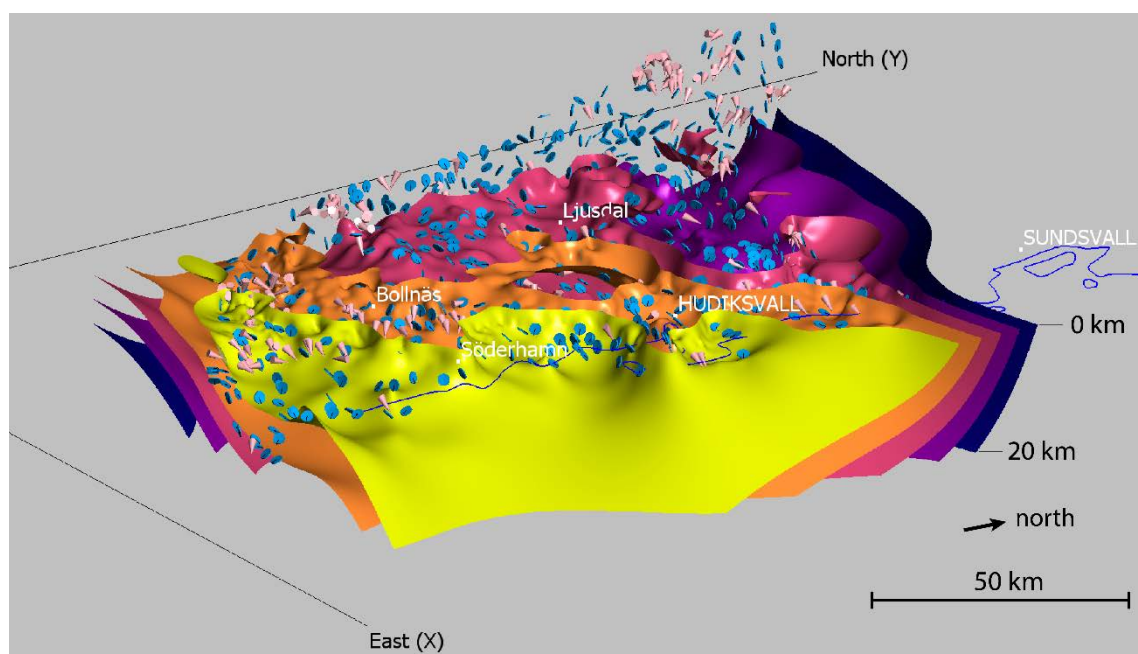


**Figure 7-6A.** Form interpolants displayed as 5 different iso-surfaces modelled from planar structural data (SGU 2023,  $n = 7\ 714$ , blue disks, not all data displayed). Fold axes ( $n = 215$ , pink cones) for display only as those cannot be included in modelling form interpolants or structural trends in Leapfrog Geo v. 2023.2. Blue line indicates shoreline of Sweden. View is to the northwest in Leapfrog Geo v. 2023.2.

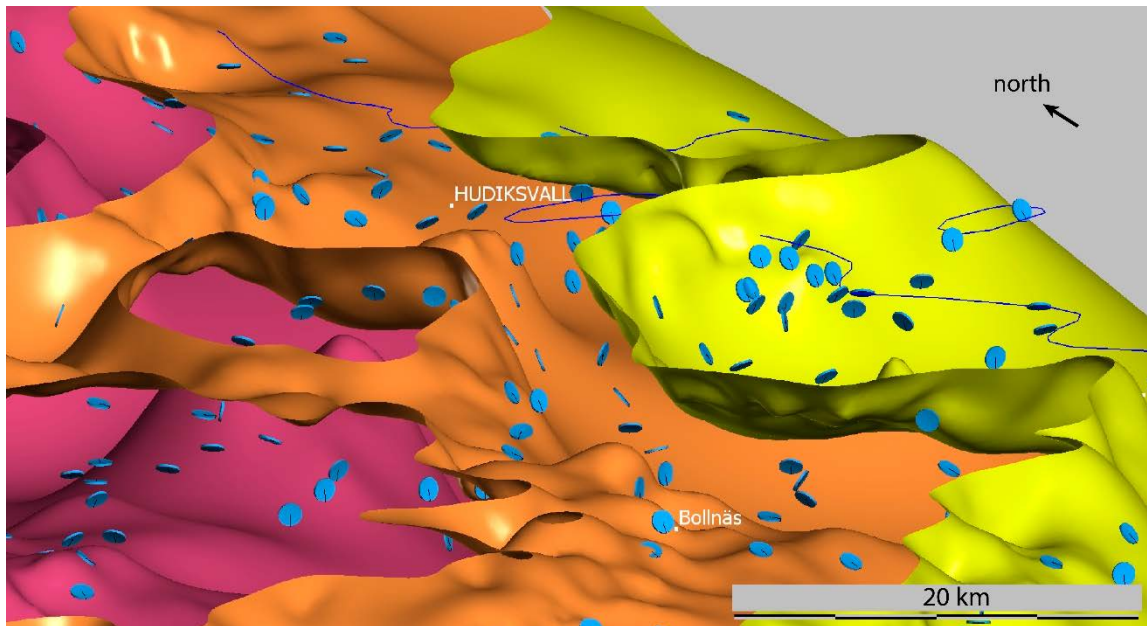


**Figure 7-6B.** Zoom-in on Figure 7-6A on the Hudiksvall area. Scene shows a “basin-and-dome” folding pattern of form interpolant iso-surfaces that were modelled from planar structural data (SGU 2023, blue disks, not all data used is displayed). Blue line indicates shoreline of Sweden. View is to the northeast in Leapfrog Geo v. 2023.2.

With ongoing modelling, form interpolants can be used to control other surfaces, such as lithological boundaries. One way to do that is by applying a “structural trend” that can be created from a selected surface(s) or structural data (Figure 7-7). A structural trend guides modelling by aligning the modelled lithology surfaces at depth to the trend direction, which was built in our case directly from the interpolant iso-surfaces. The result is that for any given point in the model, the trend orientation is specific to that location. Moreover, the structural trend we applied is of “decaying-type” and is therefore strongest along the iso-surfaces (set to 5) and decays to 0 within 5 km away from the iso-surface.

The resulting lithology model appears now more realistic than when modelled without the use of structural data. As such, the orientation of the lithological boundaries varies strongly with depth in accordance with the orientations of structural fabrics measured at the surface and the overall derived structural trend at depth (Figure 7-8).

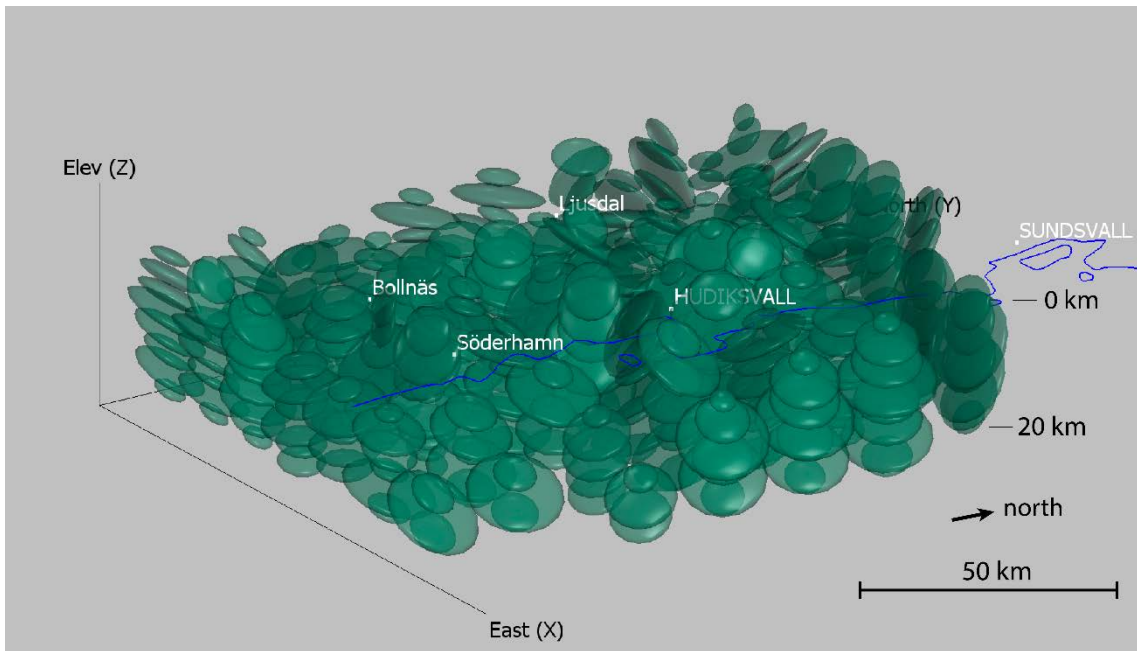


**Figure 7-7.** Structural trend displayed as a grid of oblate ellipsoids. The orientation of the disks give the direction of the anisotropy. The size of the disks is proportionally to the anisotropy strength. Note that the trend affects the entire model space and is not limited to the locations of the displayed ellipsoids. This structural trend is derived from the form interpolant iso-surfaces shown in Figure 7-2, which were in turn modelled from planar structural data (SGU 2023). The structural trend is strongest (strength 5) directly along the form interpolants decaying within a range of 5 km away from each iso-surface. Blue line indicates shoreline of Sweden. View to the west in Leapfrog Geo v. 2023.2.

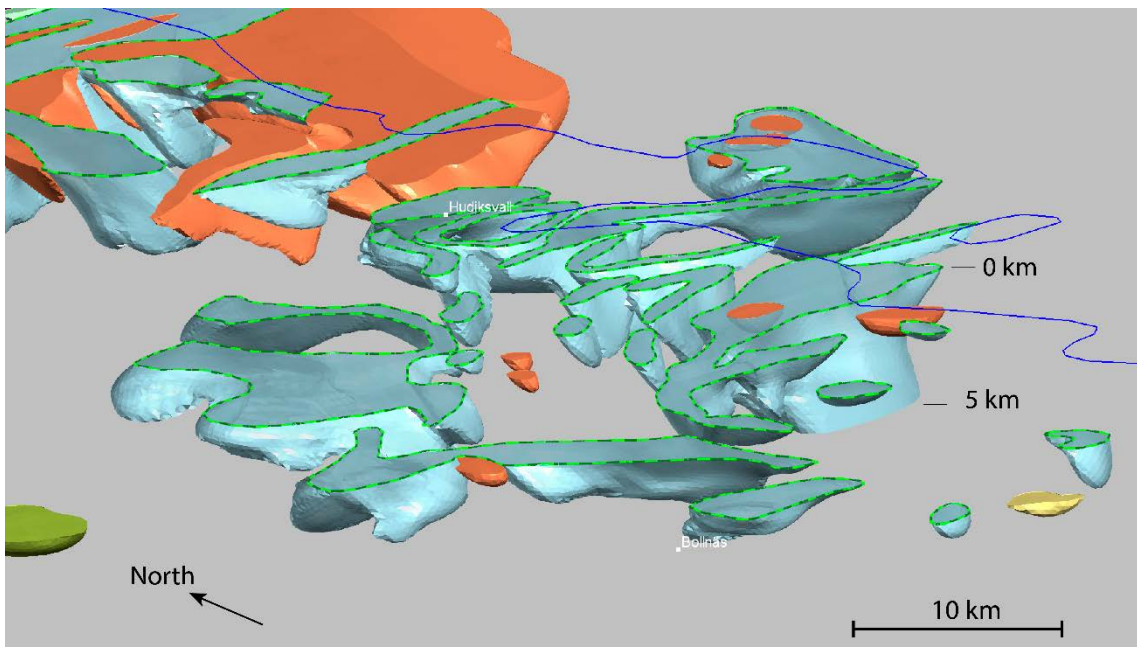


**Figure 7-8.** Zoom-in on the Hudiksvall area portraying the lithological contacts of migmatites in blueish, which were modelled as “intrusions-type” in Leapfrog Geo v. 2022.1 and constrained by map traces and a structural trend derived from planar structural measurements (see Figure 7-7). The dashed green lines represent the map traces of the migmatites as extracted from the bedrock map of Sweden at scale 1:1 million (Bergman et al. 2012; SGU 2021a). Blue line indicates shoreline of Sweden. View is to the northeast in Leapfrog Geo v. 2023.2.

## 8 Discussion and Conclusion

The 3D geological models presented in this study are first-order models and are weakly constrained at depth. They should therefore be considered conceptual or indicative more than precise and accurate. The lithology model is only very poorly constrained at depth.

Despite the lack of details, the presented models are useful as they reveal a number of important features. The crustal scale model reveals that:

- 1) A variation in crustal thickness exists throughout the modelled area. The Hudiksvall earthquake cluster appears to coincide with thickened crust (Figure 8-1). The NE-trend of this domain of thickened crust appears to match with the long axis of the earthquake cluster.
- 2) The Hagsta gneiss zone and the Hassela shear zone are southwest dipping, listric fault zones rooting into the lower crust. These zones represent respectively the northern and southern boundaries of the Ljusdal lithotectonic unit, which in our interpretation dip shallower at depth compared to the 3D model presented in Curtis et al. (2018).
- 3) Two additional crustal-scale shear zones, with similar geometries as the LTU bounding shear zones, are the Lindön shear zone and a nameless shear zone, which we refer to as Söderhamn shear zone.

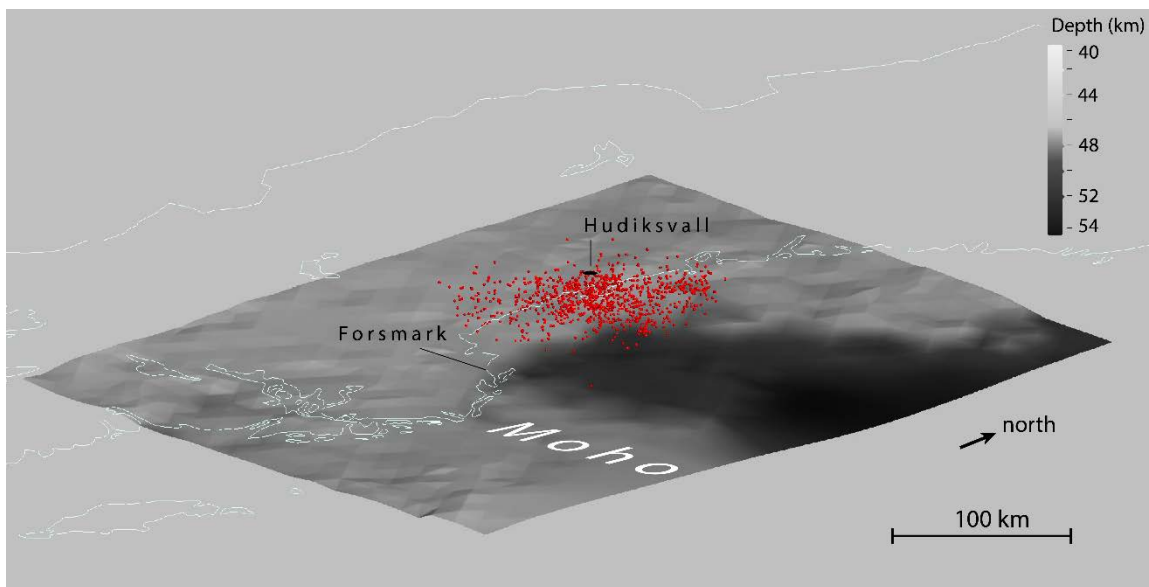


**Figure 8-1.** The Hudiksvalls earthquake cluster of recorded earthquakes occurring between 2000 and 2018 (red point cloud), overlying the Moho with a transposed color gradient corresponding to Moho depth, which is the inverse of crustal thickness. Notice the spatial correlation between the earthquake cluster and thickened crust. The thin white line indicates shorelines of Sweden. View is to the west in Leapfrog Geo v. 2023.2.

## 8.1 The “Hudiksvall fault”

An additional major northwest dipping fault, named here as “Hudiksvall fault” is inferred from interpretations on the northernmost segment of the reprocessed BABEL lines 1 and 6 (Figure 7-3). A corresponding map trace for this fault could not be found on the bedrock map of Sweden at 1:1 million (SGU 2021a) and evidence is also not directly apparent from the harmonized map presented in this study (Figure 3-2). However, additional support for the existence of the Hudiksvall fault is derived from the gravity anomaly map (Figure 6-3) and the new magnetic lineament map (Figure 6-5A). Also, the field observations on NE–SW striking pseudotachylytes provide an additional indication for faulting in association with paleo-earthquakes (Figure 4-5D). The inferred Hudiksvall fault is displayed schematically as a single surface within an alternative crustal model (Figure 8-2A), combined with the lithology model (Figure 8-2B), earthquake cluster (Figure 8-3A), and magnetic susceptibility model (Figure 8-3B). The Hudiksvall fault most likely represents a fault system comprising multiple sub-parallel shear- and fault zones (see also Figure 8-3B), which all appear to coincide with the Hudiksvall earthquake cluster and strike sub-parallel to the cluster’s long axis. Hence, we propose that the zone itself as well as its intersection with other deformation zones, such the Hassela shear zone, may play a significant role in generating the Hudiksvall earthquake cluster.

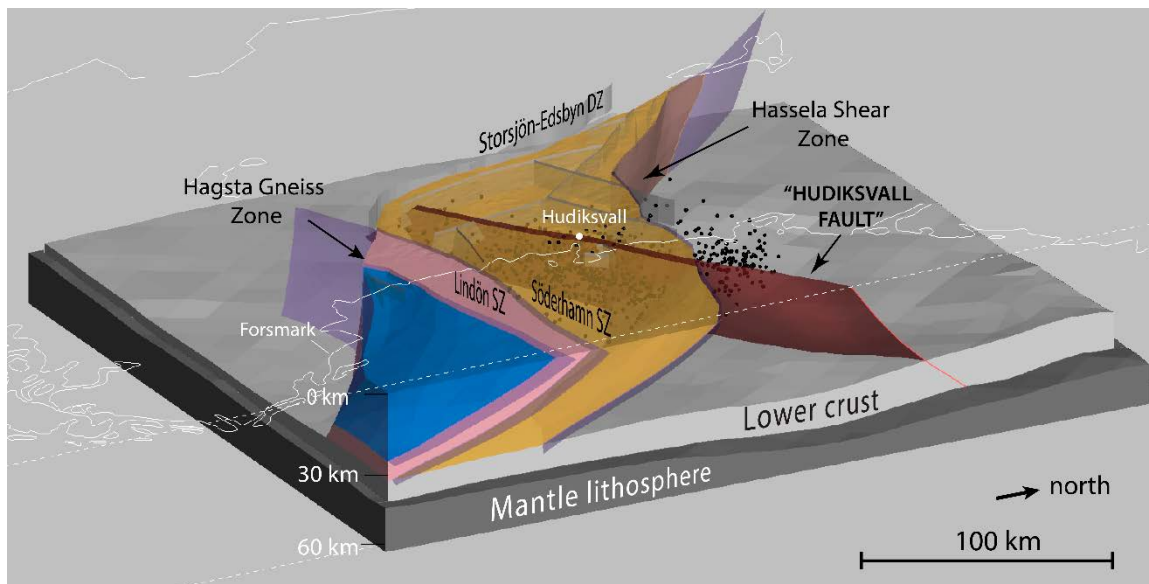


**Figure 8-2A.** An alternative model to the one presented in Figure 7-4, showing the Hudiksvall fault (red surface) which is constrained by interpretations on BABEL lines 1 and 6, field observations and geophysical modelling in this study. The modelled Hudiksvall fault coincided with the mean plane (long axis) of the Hudiksvall earthquake cluster (black point cloud). Additional minor faults in grey are from the bedrock map of Sweden 1:1 million and modelled as vertically dipping surfaces. The thin white line indicates the shorelines of Sweden. Dashes white line indicates section line for visualization. View is to the northwest in Leapfrog Geo v. 2023.2.

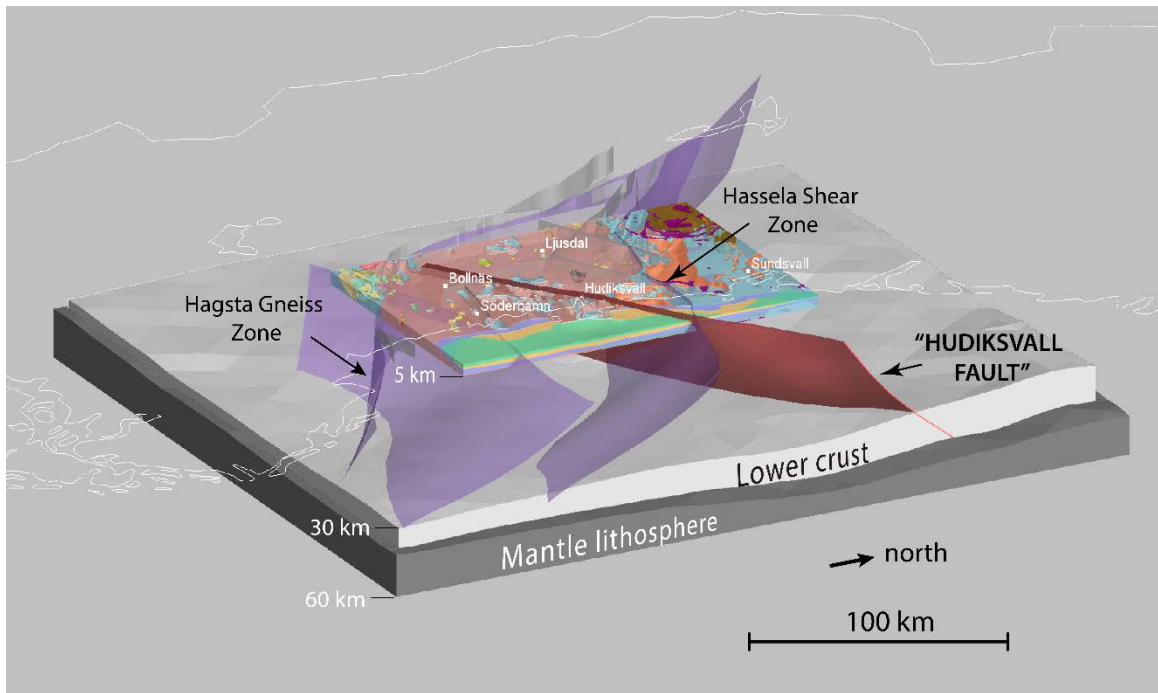


**Figure 8-2B.** Visualization combining the crustal model (see Figure 7-4) and the lithology model (see Figure 7-5). Red surface represents the Hudiksvall fault whereas the other major shear zones are colored purple. The thin white line indicates the shorelines of Sweden. Additional minor faults in grey are from the bedrock map of Sweden 1:1 million and modelled as vertically dipping surfaces. Dashed white line indicates section line and has no geological meaning. View to the west in Leapfrog Geo v. 2023.2.

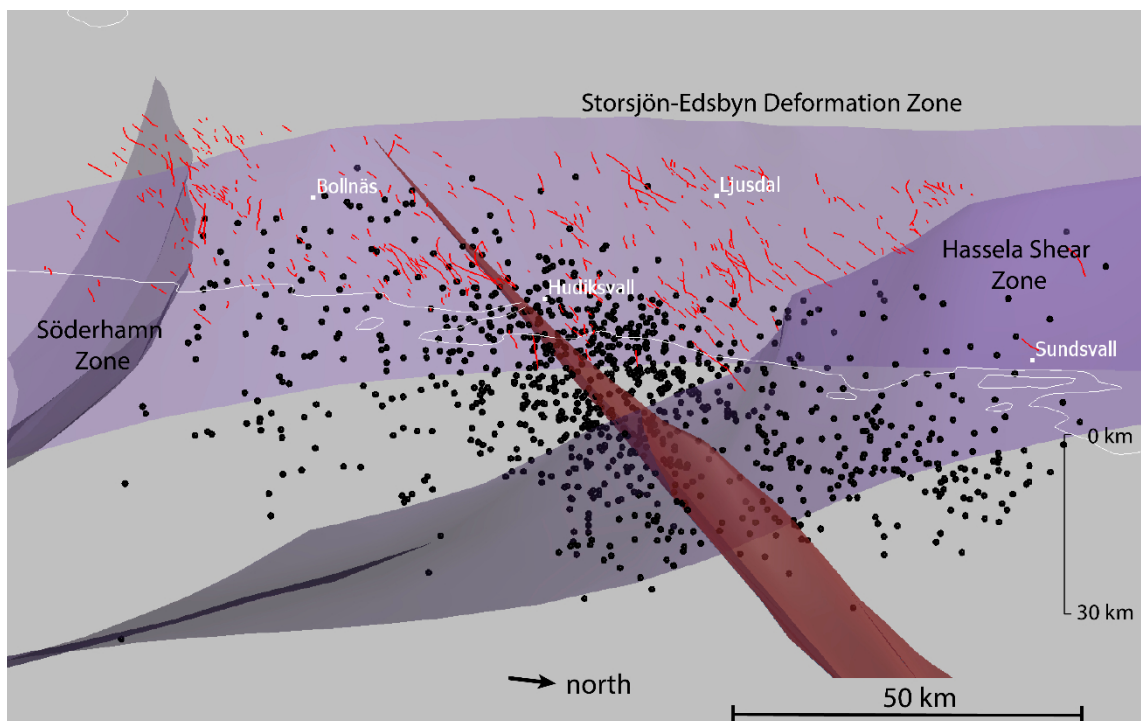


**Figure 8-3A.** The Hudiksvall fault (red surface) intersects the Hudiksvall earthquake cluster (black point cloud) and strikes sub-parallel to the cluster mean plane as well as map traces of the northeast striking lineaments (red lines) interpreted in this study from the magnetic anomaly map (see Figure 6-5A). Purple surfaces represent major shear zones. The thin white indicates the shoreline. View is to the southwest in Leapfrog Geo v. 2023.2.

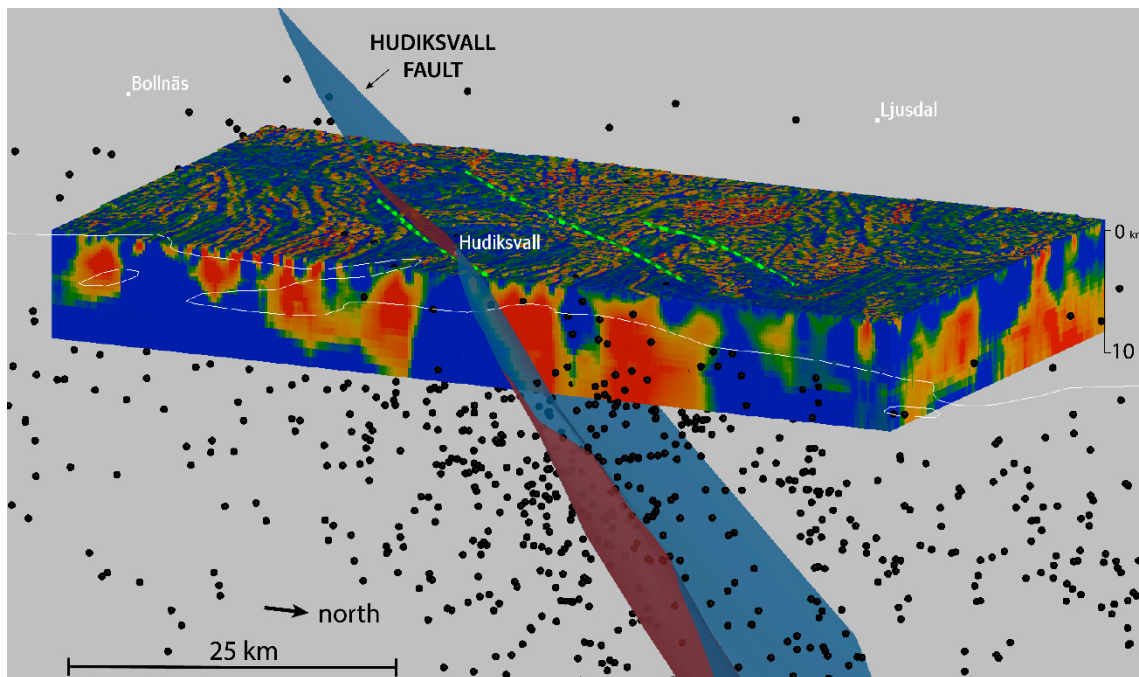


**Figure 8-3B.** Combined visualization of the Hudiksvall fault (red surface), the earthquake cluster (black dots) and the 3D susceptibility model of area i1 (Figure 6-7). The green dashed lines are major lineaments resulting from the inversion of which the southern one coincides here with the Hudiksvall fault, but the other two are likely to be part of the same fault system (Figure 6-9). The thin white indicates the shoreline. View is to the southwest in Leapfrog Geo v. 2023.2.

## 8.2 Recommendations for future work

The 3D geological models should be considered conceptual or indicative, and the lithology model in particular is very poorly constrained at depth and a refinement using additional data, such as borehole data and interpretations from gravity, magnetics and electromagnetics modelling is highly recommended for future work. It is also desirable to implement geological features shown on more detailed geological maps, such as the SGU bedrock maps at 1:50 000–250 000 scales, mainly to refine the structural pattern in the immediate surroundings of the inferred Hudiksvall fault, and to introduce faults and associated displacements of lithological boundaries. By the time of writing this report, SGU conducts a new survey of airborne geophysics in the area between Söderhamn and Ockelbo. The results will be available early 2024. Integrating results from investigations of earthquake activity using the newly installed seismological stations, especially a larger number of earthquakes with more accurately located hypocentres, would greatly improve the interpretation. Results from the seismological investigations may be used as a-priori information to help constrain future iterative geological-geophysical modelling, of which the results should be verified by targeted fieldwork.

## References

SKB's (Svensk Kärnbränslehantering AB) publications can be found at [www.skb.com/publications](http://www.skb.com/publications).

**Allmendinger R W, Cardozo N, Fisher D, 2012.** Structural geology algorithms: Vectors and tensors in structural geology: Cambridge University Press.

**Angelier J, Mechler P, 1977.** Sur une méthode graphique de recherche des contraintes principales également utilisable en tectonique et en séismologie: la méthode des dièdres droits. Bulletin de la Société géologique de France (In French.)

**BABEL Working Group, 1990.** Evidence for Early Proterozoic plate tectonic from seismic reflection profiles in the Baltic Shield. *Nature* 348, 34–38.

**BABEL Working Group, 1993.** Integrated seismic studies of the Baltic Shield using data in the Gulf of Bothnia region. *Geophys. J. Int.* 112, 305–324.

**Bergman S, Sjöström H, 1994.** The Storsjön-Edsbyn Deformation Zone, central Sweden. Unpublished research report, 1-46. <http://urn.kb.se/resolve?urn=urn:nbn:se:uu:diva-331133>

**Bergman S, Sjöström H, Högdahl K, 2006.** Transpressive shear related to arc magmatism: The Paleoproterozoic Storsjön-Edsbyn Deformation Zone, central Sweden. *Tectonics* 25, 1–16.

**Bergman S, Stephens M B, Andersson J, Kathol B, Bergman T, 2012.** Bedrock map of Sweden, scale 1:1 million. Sveriges geologiska undersökning K 423.

**Buntin S, 2021.** Seismic structure of the central Svecofennian lithosphere. Doctoral dissertation, Acta Universitatis Upsaliensis.

**Buntin S, Malehmir A, 2021.** Velocity structure of the Fennoscandian Shield through ray tracing modelling of FENNOLOGRA and UPPLAND seismic profiles. In “Seismic structure of the central Svecofennian lithosphere”. Doctoral dissertation, Acta Universitatis Upsaliensis.

**Buntin S, Malehmir A, Koyi H, Högdahl K, Malinowski M, Larsson S Å, Tybo H, Juhlin C, Korja A, Górszczyk A, 2019.** Emplacement and 3D geometry of crustal-scale saucer-shaped intrusions in the Fennoscandian Shield. *Scientific Reports*, 9, 10498.

**Buntin S, Artemieva I M, Malehmir A, 2021.** Long-lived Paleoproterozoic eclogitic lower crust. *Nature Communications* 12, 655. <https://doi.org/10.1038/s41467-021-26878-5>

**Cardozo N, Allmendinger R W, 2013.** Spherical projections with OSXStereonet: *Computers & Geosciences*, 51, 193–205. doi:10.1016/j.cageo.2012.07.021

**Curtis P, Wahlgren C H, Bergman S, Antal Lundin I, Mellqvist C, Luth S, Olsson S, 2018.** 3D Model of Lithotectonic Units and Regional Deformation Zones in the Bedrock of Sweden. Sveriges Geologiska Undersökning Rapport 2018: 06, 55.

**Delvaux D, Sperner B, 2003.** New aspects of tectonic stress inversion with reference to the TENSOR program. *Geological Society of London Special Publications* 212 (1): 75.

**Seequent, 2022.** Geosoft Oasis Montaj with VOXI extension, version 2022.2. Available at: <https://www.seequent.com/products-solutions/geosoft-oasis-montaj/> [26 September 2024].

**GFZ, 2023.** World Stress map. Helmholtz Centre Potsdam GFZ German Research Centre for Geosciences. <[www.world-stress-map.org](http://www.world-stress-map.org)>, 2023-12-15.

**Grad M, Tiira T, ESC Working Group, 2009.** The Moho depth map of the European Plate, *Geophysical Journal International* 176, 279–292. doi: 10.1111/j.1365-246X.2008.03919.x

**Heikkinen P, Luosto U, 1992.** Velocity structure and reflectivity of the Proterozoic crust in the Bothnian Sea. In: Meissner, R., Snyder, D., Balling, N., Staroste, E. (Eds.), *The BABEL Project, First Status Report*, EUR 14429. Commission of the European Communities, Directorate-General, Science, Research and Development, Brussels, pp. 65–69.

**Högdahl K, Bergman S, 2020.** Paleoproterozoic (1.9–1.8 Ga), syn-orogenic magmatism and sedimentation in the Ljusdal lithotectonic unit, Svecofennian orogen. *Geological Society, London, Memoirs*, 50(1), 131–153.

- Högdahl K, Sjöström H, 2001.** Evidence for 1.82 Ga transpressive shearing in a 1.85 Ga granitoid in central Sweden: implications for the regional evolution. *Precambrian Research*, 105(1), 37–56.
- Högdahl K, Sjöström H, Bergman S, 2009.** Ductile shear zones related to crustal shortening and domain boundary evolution in the central Fennoscandian Shield, *Tectonics*, 28, TC1003, doi:10.1029/2008TC002277
- Korja A, Heikkinen P, 2005.** The accretionary Svecofennian orogen-insight from the BABEL profiles. *Precambrian Research* 136, 241–268.
- Korja A, Heikkinen P, Aaro S, 2001.** Crustal structure of the northern Baltic Sea paleorift. *Tectonophysics* 331, 341–358.
- Leapfrog Geo, 2023.** <https://www.seequent.com/products-solutions/leapfrog-geo>
- Matthews P A, Graham D P, Long R E, 1992.** Crustal structure beneath BABEL line 6 from wide-angle and normal-incidence seismic reflection data. In: Meissner, R., Snyder, D., Balling, N., Staroste, E. (Eds.), *The BABEL Project, First Status Report*, EUR 14429. Commission of the European Communities, Directorate-General, Science, Research and Development, Brussels, pp. 101–104.
- Ogenhall E, Sjöström H, 2010.** Deformation history of the Palaeoproterozoic Svecofennian supracrustal rocks at Hamrånge, south-central Sweden. In Ogenhall, E. *Geological Evolution of the Supracrustal Palaeoproterozoic Hamrånge Group: A Svecofennian Case Study*. Acta Universitatis Upsaliensis Uppsala, Uppsala University.
- Saintot A, Stephens M B, Viola G, Nordgulen Ø, 2011.** Brittle tectonic evolution and paleostress field reconstruction in the southwestern part of the Fennoscandian Shield, Forsmark, Sweden. *Tectonics*, 30(4).
- SGU, 2021a.** Bedrock 1:1 million – database. Southern Norrland. 2021-11-25.
- SGU, 2021b.** Bedrock 1:50 000–1:250 000 – database. Hudiksvall area. 2021-11-25.
- SGU, 2023.** Bedrock observations – database. Hudiksvall area. 2023-04.
- Sjöström H, Högdahl K, Aaro S, Bergman S, 2000.** The Hassela shear zone in central Sweden, the western part of a Palaeoproterozoic tectonic domain boundary across the Baltic Shield?. In E. Eide (ed): *Abstract volume*, 24. Nordiske Geologiske Vintermöte, Trondheim. *Geonytt* 1, 153.
- Skyttä P, Weihed P, Högdahl K, Bergman S, Stephens M B, 2020.** Paleoproterozoic (2.0–1.8 Ga), syn-orogenic sedimentation, magmatism and mineralization in the Bothnia-Skellefteå lithotectonic unit, Svecofennian orogen. *Geological Society, London, Memoirs*, 50, 83–130.
- Smith C A, Sundh M, Mikko H, 2014.** Surficial geology indicates early Holocene faulting and seismicity, central Sweden. *International Journal of Earth Sciences* 103, 1711–1724, doi: 10.1007/s00531-014-1025-6
- Stephens M B, 2020.** Introduction to the lithotectonic framework of Sweden and organization of this Memoir. *Geological Society, London, Memoirs*, 50, 1–15.
- Stephens M B, Fox A, La Pointe P, Simeonov A, Isaksson H, Hermanson J, Öhman J, 2007.** *Geology Forsmark. Site descriptive modelling Forsmark stage 2.2*. SKB R-07-45.
- Svensson N B, 1968.** The Dellen lakes, a probable meteorite impact in central Sweden. *Geologiska Föreningens i Stockholm Förhandlingar* 90, 314–316.
- Söderbäck B (ed), 2008.** Geological evolution, paleoclimate and historical development of the Forsmark and Laxemar-Simpevarp areas. *Site descriptive modelling, SDM-Site*. SKB R-08-19, Svensk Kärnbränslehantering AB.
- Viola G, Venvik Ganerød G, Wahlgren C H, 2009.** Unraveling 1.5 Ga of brittle deformation history in the Laxemar-Simpevarp area, southeast Sweden: A contribution to the Swedish site investigation study for the disposal of highly radioactive nuclear waste. *Tectonics*, 28(5).
- WinTensor, 2023.** <http://damiendelveaux.be/Tensor/UserGuides>

## Appendix

**Table A-1. Location coordinates of studied outcrops for structural measurements. Coordinates are in SWEREF99 TM.**

OBSERVATION	NORTH (m)	EAST (m)	ELEVATION (m)
SLH210001	6837810	606939	59
SLH210002	6835000	607806	56
SLH210003	6840588	610605	47
SLH210004	6840715	613567	52
SLH210005	6849027	593559	96
SLH210006	6846770	598341	55
SLH210007	6844889	605434	72
SLH210008	6845493	606773	99
SLH210009	6878253	617000	116
SLH210010	6878333	616943	141
SLH210011	6878191	616979	128
SLH210012	6904657	627357	62
SLH210013	6902971	638228	6
SLH210014	6873372	614277	94
SLH210015	6847143	609586	49
SLH210016	6846485	609281	65
SLH210017	6846166	609192	64
SLH210018	6845164	609022	58
SLH210019	6793300	597119	88
SLH210020	6792490	583302	57
SLH210021	6795047	581083	68
SLH210022	6796351	576613	163
SLH210023	6825407	571611	151
SLH210024	6844251	608278	132
SLH210025	6852283	612717	63
SLH210026	6851982	612580	67
SLH210027	6851451	612238	78
SLH210028	6841626	609785	43
SLH210029	6842167	609658	34
SLH210030	6842671	609608	32
SLH210031	6871121	578445	222
SLH210032	6871323	578359	236
SLH210033	6871379	578196	235
SLH210034	6868482	582595	244
SLH210035	6856682	597712	108
SLH210036	6855228	595847	66
SLH210037	6848929	599840	60
SLH210038	6859239	607484	91
SLH210039	6861010	607890	100
SLH210040	6866605	606904	125
SLH210041	6876588	608946	66
SLH210042	6881210	611763	100
SLH210043	6894370	621201	168
SLH210044	6895571	621888	148
SLH210045	6834502	629344	20
SLH210046	6840800	626495	79
SLH210047	6844318	624108	42
SLH210048	6831540	606252	44

**Table A-2. Orientation of fault planes, slip-lines and slip sense. Collected structural data used for paleostress analysis presented in this study. Slip sense R: reverse, N: normal, D: dextral, S: sinistral, I: oblique slip. Confidence level: C: certain, P: probable, S: supposed.**

Structure_ID	Outcrop cluster	Plane strike	Plane dip	Slip line plunge	Slip line trend	Slip sense	Confidence level
SLH210001_1	1	70	66	22	240	I	P
SLH210001_11	1	244	44	25	28	N	S
SLH210001_12	1	190	84	54	200	N	S
SLH210001_2	1	63	70	43	225	N	C
SLH210001_4	1	320	84	20	130	I	P
SLH210001_5	1	260	22	22	340	N	P
SLH210001_6	1	80	75	62	230	R	P
SLH210001_7	1	155	82	62	170	N	P
SLH210001_8	1	338	85	12	158	S	C
SLH210001_9	1	30	82	60	180	I	S
SLH210048_1	1	290	52	42	0	I	C
SLH210048_10	1	342	60	0	342	S	S
SLH210048_2	1	335	45	12	5	N	C
SLH210048_3	1	76	50	40	100	N	S
SLH210048_4	1	15	56	0	12	S	S
SLH210048_5	1	175	89	38	355	I	S
SLH210003_1	2	64	60	60	150	R	C
SLH210004_1	2	274	86	64	300	R	C
SLH210004_2	2	275	85	33	282	N	C
SLH210004_3	2	223	86	85	312	N	C
SLH210004_4	2	15	54	5	195	S	P
SLH210004_5	2	286	80	12	292	N	P
SLH210028_1	2	338	53	34	5	N	P
SLH210028_2	2	120	88	12	125	N	C
SLH210028_4	2	3	68	12	12	N	S
SLH210028_9	2	347	78	3	170	I	S
SLH210029_1	2	336	64	6	148	I	C
SLH210029_2	2	35	53	28	180	I	P
SLH210029_3	2	17	78	70	180	I	S
SLH210030_4	2	250	74	0	250	S	B
SLH210007_1	3	205	80	40	22	N	C
SLH210007_11	3	262	68	34	272	I	P
SLH210007_12	3	255	80	24	70	I	C
SLH210007_13	3	184	64	4	192	I	P
SLH210007_14	3	58	63	53	193	N	C
SLH210007_15	3	34	75	37	192	N	C
SLH210007_16	3	47	72	62	190	N	S
SLH210007_17	3	30	72	60	173	N	C
SLH210007_18	3	110	89	38	110	N	S
SLH210007_19	3	40	66	54	185	N	P
SLH210007_2	3	242	56	34	46	N	C
SLH210007_3	3	258	37	13	58	N	C
SLH210007_4	3	128	89	32	305	I	C
SLH210007_5	3	215	84	45	25	N	C
SLH210007_6	3	265	43	12	68	N	C
SLH210007_7	3	105	45	6	275	N	C
SLH210007_8	3	47	50	20	70	N	P
SLH210007_9	3	106	88	67	132	N	P
SLH210005_1	4	287	58	13	295	I	C
SLH210005_10	4	285	89	76	292	I	C
SLH210005_11	4	290	88	74	108	I	C
SLH210005_12	4	88	86	52	257	N	P

**Table A-2. Continued.**

Structure_ID	Outcrop cluster	Plane strike	Plane dip	Slip line plunge	Slip line trend	Slip sense	Confidence level
SLH210005_13	4	234	54	34	266	I	C
SLH210005_14	4	352	77	56	172	I	S
SLH210005_15	4	10	86	70	180	I	S
SLH210005_2	4	240	64	28	50	I	C
SLH210005_3	4	92	88	62	110	N	P
SLH210005_4	4	188	83	70	220	N	S
SLH210005_5	4	172	84	62	176	N	S
SLH210005_6	4	100	72	54	170	N	P
SLH210005_7	4	112	86	84	155	N	P
SLH210005_8	4	170	74	67	206	N	C
SLH210006_1	4	298	72	54	47	N	C
SLH210006_10	4	153	86	67	320	I	P
SLH210006_11	4	246	46	35	35	N	P
SLH210006_12	4	125	85	58	140	I	P
SLH210006_13	4	110	73	46	133	I	C
SLH210006_14	4	214	50	48	322	I	S
SLH210006_15	4	275	75	68	50	N	C
SLH210006_17	4	312	89	10	314	S	C
SLH210006_2	4	110	89	35	290	I	S
SLH210006_3	4	18	55	48	60	N	C
SLH210006_4	4	325	85	50	335	N	S
SLH210006_5	4	60	62	56	96	I	C
SLH210006_9	4	335	88	32	155	N	P
SLH210018_1	5	255	77	4	72	I	C
SLH210018_11	5	205	70	21	20	I	P
SLH210018_2	5	145	27	24	220	N	P
SLH210018_3	5	143	56	37	185	I	P
SLH210018_4	5	139	45	38	212	N	C
SLH210018_5	5	82	73	48	105	N	C
SLH210018_6	5	255	86	47	67	I	S
SLH210018_7	5	222	88	22	37	I	C
SLH210018_8	5	47	84	12	50	N	S
SLH210018_9	5	90	84	42	105	N	S
SLH210024_1	5	170	43	12	327	I	C
SLH210024_10	5	182	88	28	355	I	P
SLH210024_2	5	263	84	70	65	I	P
SLH210024_3	5	269	84	70	345	I	S
SLH210024_5	5	314	82	3	314	I	C
SLH210024_6	5	184	50	38	275	I	C
SLH210024_7	5	182	46	46	270	R	C
SLH210024_8	5	344	89	65	165	N	S
SLH210015_1	6	357	85	63	158	I	P
SLH210015_2	6	44	87	39	50	I	S
SLH210015_3	6	6	87	45	12	I	P
SLH210015_4	6	135	84	60	300	N	P
SLH210015_5	6	158	84	65	330	N	S
SLH210015_6	6	310	86	5	318	D	C
SLH210015_7	6	326	74	32	135	I	P
SLH210015_8	6	40	82	12	45	I	C
SLH210015_9	6	46	88	4	50	I	C
SLH210016_1	6	320	70	21	327	I	P
SLH210016_3	6	148	87	24	340	N	C
SLH210016_7	6	250	37	33	290	N	P
SLH210016_8	6	182	73	27	355	N	C

**Table A-2. Continued.**

Structure_ID	Outcrop cluster	Plane strike	Plane dip	Slip line plunge	Slip line trend	Slip sense	Confidence level
SLH210016_9	6	240	21	7	47	N	P
SLH210017_1	6	18	78	58	38	I	C
SLH210017_2	6	12	77	38	27	I	P
SLH210017_3	6	222	88	27	228	N	P
SLH210017_4	6	160	73	29	332	N	S
SLH210017_5	6	38	43	20	58	N	P
SLH210017_6	6	257	56	52	326	I	S
SLH210025_1	7	20	89	80	198	N	P
SLH210025_3	7	196	78	73	220	N	S
SLH210025_5	7	290	73	32	100	I	C
SLH210025_6	7	260	62	38	45	N	P
SLH210026_10	7	18	78	75	140	I	S
SLH210026_2	7	220	74	74	310	R	P
SLH210026_5	7	352	67	64	125	N	C
SLH210019_1	8	253	83	18	68	I	C
SLH210019_10	8	46	80	47	203	N	C
SLH210019_11	8	133	44	44	216	R	P
SLH210019_14	8	70	63	48	194	I	P
SLH210019_15	8	200	87	37	210	N	P
SLH210019_2	8	220	72	42	242	I	P
SLH210019_3	8	290	57	52	16	N	S
SLH210019_4	8	68	89	17	78	N	C
SLH210019_7	8	85	70	67	202	I	C
SLH210019_8	8	198	65	38	210	I	S
SLH210019_9	8	50	83	50	295	N	S

SKB is responsible for managing spent nuclear fuel and radioactive waste produced by the Swedish nuclear power plants such that man and the environment are protected in the near and distant future.

**skb.se**